

1 **Bowen ratio-constrained global dataset of bulk air-sea turbulent**
2 **heat fluxes from 1993 to 2017**

3 Yizhe Wang^{a, b}, Ronglin Tang^{a, b, *}, Meng Liu^c, Lingxiao Huang^{a, b}, Zhao-Liang Li^{a, b, c}

4 ^a State Key Laboratory of Resources and Environment Information System, Institute of
5 Geographic Sciences and Natural Resources Research, Chinese Academy of Sciences,
6 Beijing 100101, China

7 ^b University of Chinese Academy of Sciences, Beijing 100049, China

8 ^c State Key Laboratory of Efficient Utilization of Arable Land in China, Institute of
9 Agricultural Resources and Regional Planning, Chinese Academy of Agricultural
10 Sciences, Beijing 100081, China

11 * Authors to whom correspondence should be addressed: tangrl@reis.ac.cn

12

13

14

15 **Abstract**

16 Air-sea turbulent heat fluxes, including the sensible heat flux (SHF) and latent heat
17 flux (LHF), along with the Bowen ratio (β , ratio of SHF to LHF), are crucial for
18 understanding air-sea interaction and global energy and water budgets. However, the
19 existing products, primarily developed using the semi-empirical bulk aerodynamic
20 methods and data-driven machine learning approaches, are often weak in accuracy and
21 physical rationality, due to the uncertainties in the environmental forcings and
22 inappropriate parameterizations. In this study, we generated a global daily 0.25° product
23 of **bulk** air-sea turbulent heat fluxes using the Bowen ratio-constrained Neural Network
24 (NN) model (referred to as the BrTHF model) that could coordinately estimate the SHF
25 and LHF, along with the observations from 197 globally distributed buoys and multi-
26 source remote sensing and reanalysis **foreinginputs**. The spatial ten-fold cross-
27 validation results showed that the BrTHF model, achieving root mean square errors of
28 6.05 W/m^2 , 23.67 W/m^2 and 0.22 and correlation coefficients of 0.93 , 0.91 and 0.25 for
29 the SHF, LHF and β , respectively, outperformed the physics-agnostic NN model and
30 seven widely used air-sea turbulent heat flux products (including JOFURO3,
31 IFREMER, SeaFlux, ERA5, MERRA2, OAFflux, and OHF). Furthermore, the inter-
32 comparison of the spatial distribution of multi-year means, as well as intra-annual and
33 inter-annual change patterns showed that the BrTHF product reliably simulated global
34 SHF, LHF and β , in contrast to the machine learning-based OHF product that failed to
35 replicate these patterns. The main advantage of the BrTHF model lies in its improved
36 rationality of β estimates, successfully eliminating the outliers observed in the physics-
37 agnostic NN model and the seven typical products. The improved SHF, LHF, and β
38 estimates can allow for more accurate quantification of the global air-sea energy and
39 water budgets, enhance our understanding of air-sea interaction, and improve
40 projections of climate change under global warming. The 0.25° daily global product
41 from 1993 to 2017 can be freely accessed from the National Tibetan Plateau Data
42 Center (TPDC) [<https://doi.org/10.11888/Atmos.tpdc.302578>, Tang and Wang (2025)].

43 **Keywords:** Air-sea turbulent heat fluxes; Sensible heat flux; Latent heat flux; Bowen
44 ratio

45 **1. Introduction**

46 Air-sea turbulent heat fluxes (~~THF~~), comprising the ~~evaporative~~ latent heat flux
47 (LHF) and ~~conductive~~ sensible heat flux (SHF), play vital roles in the Earth's climate
48 system by characterizing the exchange of energy and water between the ocean and
49 atmosphere (Wild et al., 2014; Loeb et al., 2021; Fasullo et al., 2014). ~~The ratio,~~
50 ~~commonly referred to as the Bowen Ratio ($\beta = \text{SHF}/\text{LHF}$), serves as a key indicator~~
51 ~~revealing the partitioning of water and energy over the ocean and atmosphere (Jo, 2002;~~
52 ~~Andreas et al., 2013; Liu and Yang, 2021).~~ Accurate estimation of SHF, LHF and their
53 ratio—the Bowen ratio ($\beta = \text{SHF}/\text{LHF}$) ~~these three parameters~~ is an essential
54 prerequisite for advancing our understanding of —atmosphere-sea interaction
55 (Gentemann et al., 2020), improving the quantification of global water and energy
56 budget (Zhang, 2023), and enhancing the predictability of extreme weather events (Yu,
57 2019).

58 To estimate global air-sea turbulent heat fluxes, the semi-empirical bulk
59 aerodynamic method was developed based on the Monin-Obukhov similarity theory
60 (Monin and Obukhov, 1954). It establishes scaling relationships between fluxes and
61 near-surface meteorological variables such as wind speed, humidity, and temperature
62 (Yu, 2019). ~~To map global air-sea turbulent heat fluxes, the semi-empirical bulk~~
63 ~~aerodynamic method, which establishes scaling relationships between flux and profiles~~
64 ~~of easily measured mean metrological quantities, such as near surface gradients of~~
65 ~~humidity, temperature and wind (Yu, 2019), based on the Monin-Obukhov similarity~~
66 ~~theory (Monin and Obukhov, 1954), was developed and widely adopted as a primary~~
67 ~~approach.~~ This method, for its ease of application, has been applied to generate tens of
68 widely used products in the past few decades (Shie et al., 2009; Liman et al., 2018; Yu
69 and Weller, 2007; Berry and Kent, 2011; Tomita et al., 2018; Crespo et al., 2019).
70 However, there were huge discrepancies in the global and regional magnitude and

71 patterns of SHF and LHF among these products, which seriously ~~impeded~~ ~~imped~~ our
72 understanding of the key process of the air-sea interaction and the global budget of
73 water and energy (Bentamy et al., 2017; Tang et al., 2024; Yu, 2019). The discrepancies
74 could be partly ~~attributed~~ ~~described~~ to the substantial uncertainties in the environmental
75 forcings used to develop these products (Robertson et al., 2020) and the inappropriate
76 parameterizations ~~regarding regional atmospheric stability and boundary layer~~
77 ~~dynamics, across diverse and complex environmental conditions~~ (Brodeau et al., 2017;
78 Jiang et al., 2024a; Jiang et al., 2024b; Yang et al., 2024). More explicitly, existing
79 parameterizations often rely on simplified assumptions about atmospheric stability and
80 boundary layer dynamics, which may not hold under diverse environmental conditions.
81 For instance, most bulk algorithms are optimized for moderate wind regimes, resulting
82 in degraded performance and increased uncertainty when applied under weak wind
83 regimes (Jiang et al., 2024a; Brunke, 2002). At very high wind speeds, however,
84 observations show that the drag coefficient can decrease due to sea spray and whitecap
85 formation, reducing effective surface roughness and potentially biasing flux estimates
86 (Cai et al., 2025). In addition, simplifications in the treatment of sea surface skin
87 temperature, saturation humidity, and air density in the parameterizations can also
88 introduce substantial uncertainty (Brodeau et al., 2017). Together, these limitations can
89 contribute ~~—Furthermore, these problems contribute~~ a lot to the biases in the SHF and
90 LHF estimates which can even lead to the unphysical estimations of β , as Wang et al.
91 (2024) reported. To better describe and comprehend the air-sea interaction and the
92 energy and water budgets, the existing mode to produce global air-sea turbulent heat
93 fluxes needs improvement urgently.

94 Machine learning techniques have been extensively applied to upscale point-scale
95 in-situ measurements of a single variable (such as soil moisture, roughness, or
96 temperature) into grid-scale global datasets ~~in up-scaling in situ measurements of a~~
97 ~~single variable (e.g. soil moisture, roughness or temperature) to the globe~~ (Wang et al.,
98 2023; Peng et al., 2022; O and Orth, 2021; Nelson et al., 2024; Fu et al., 2023). These

99 efforts highlight the great potential of machine learning for more accurate and
100 consistent multivariate coordinated mapping (Karniadakis et al., 2021; Kashinath et al.,
101 2021; Van Der Westhuizen et al., 2023; Wang et al., 2024). However, the application of
102 machine learning in global mapping of air-sea turbulent heat fluxes remains limited.
103 Among these studies, some have focused on solely improving the accuracy of LHF
104 (Bourras et al., 2002; Chen et al., 2020b; Bourras et al., 2003), while the remaining
105 studies have mostly considered independent modeling of SHF and LHF (Bourras et al.,
106 2007; Cummins et al., 2024; Cummins et al., 2023; Zhou et al., 2024). In both
107 approaches, however, most studies have not produced long-term flux products. –The
108 only publicly available machine learning-based global air-sea turbulent heat fluxes
109 product, released by the National Oceanic and Atmospheric Administration (NOAA)
110 Ocean heat flux CDR (hereafter dubbed OHF), simultaneously modeled SHF and LHF
111 using a Neural Network (NN) technique (Clayson and Brown, 2016). Although it
112 performed well when validated against the observations from the tropical buoys, it
113 failed to capture the regional characteristics, particularly in areas where air-sea
114 turbulent heat exchange is intense (e.g. oceans with latitudes beyond 45° for SHF and
115 subtropical highs for LHF) (Tang et al., 2024). Additionally, it exhibited different
116 patterns of temporal evolution of global annual mean and opposite inter-annual trends
117 at both regional and global scales to most widely-used physical model-based products,
118 likely due to unreasonable construction of observation datasets [with data before and
119 after 2007 coming from SeaFlux in-situ datasets and ICOADS (International
120 Comprehensive Ocean-Atmosphere Data Set) datasets, respectively]. Furthermore, the
121 product likely suffers from unphysical estimates of the β due to neglecting the
122 interrelations among SHF, LHF and β during the model construction.

123 To improve the estimation of SHF, LHF, and β in a coordinative framework, we
124 recently proposed an innovative Bowen ratio-informed data-driven model by
125 considering their synergistic changes [on the one hand, ensuring physical consistency
126 (i.e., $\text{SHF/LHF} = \beta$); on the other hand, achieving high-accuracy estimations of SHF,

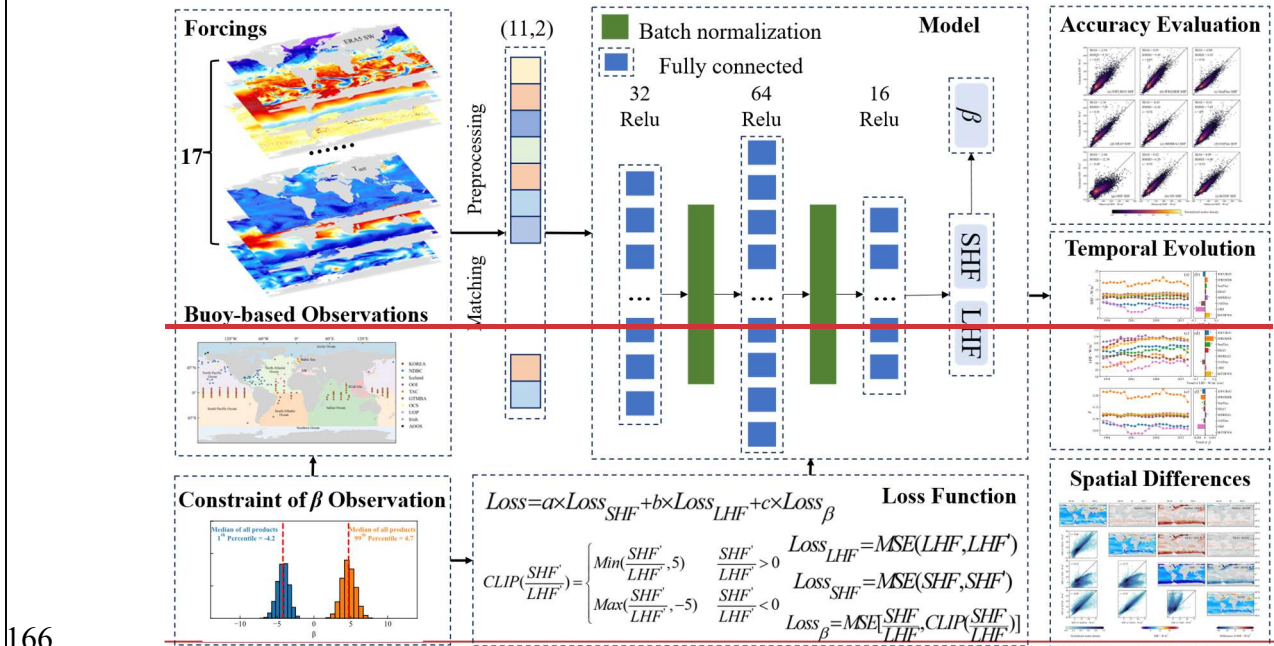
127 LHF, and β simultaneously] using a Random Forest (RF) technique (Wang et al., 2024).
128 Validation against hourly ~~high-quality~~ eddy covariance (EC) flux measurements from
129 53 historical cruises demonstrated the model's superior performance, achieving high
130 accuracy in estimating SHF, LHF, and β , with results that are physically consistent.
131 Wang et al. (2024) ~~This work~~ highlights the feasibility of simultaneously estimating
132 SHF, LHF, and β with high accuracy using machine learning techniques, offering strong
133 potential for global mapping that aligns with physical consistency. ~~However, due to~~
134 ~~limited availability of EC flux measurements (characterized by sparse spatio-temporal~~
135 ~~distributions), the application of the model for global mapping remains constrained.~~
136 However, since EC observations are difficult to obtain at sea due to platform motion
137 and airflow distortion (Bourras et al., 2019; Bourras et al., 2009) ~~—their limited spatio-~~
138 ~~temporal coverage constrains the application of the model for global mapping.~~ Buoy-
139 based flux observations provide a viable alternative. ~~Although less reliable than EC-~~
140 ~~based flux measurements,~~ B buoy data offer globally representative flux samples with
141 adequate volume and acceptable accuracy, which have been widely used to evaluate the
142 performance of global products (Bentamy et al., 2017; Bourras, 2006; Tang et al., 2024;
143 Weller et al., 2022; Zhou et al., 2020) ~~(Bentamy et al., 2017; Tang et al., 2024; Weller~~
144 ~~et al., 2022; Zhou et al., 2020)~~ and support global modeling (Chen et al., 2020a) and
145 analysis (Song et al., 2024; Yan et al., 2024).

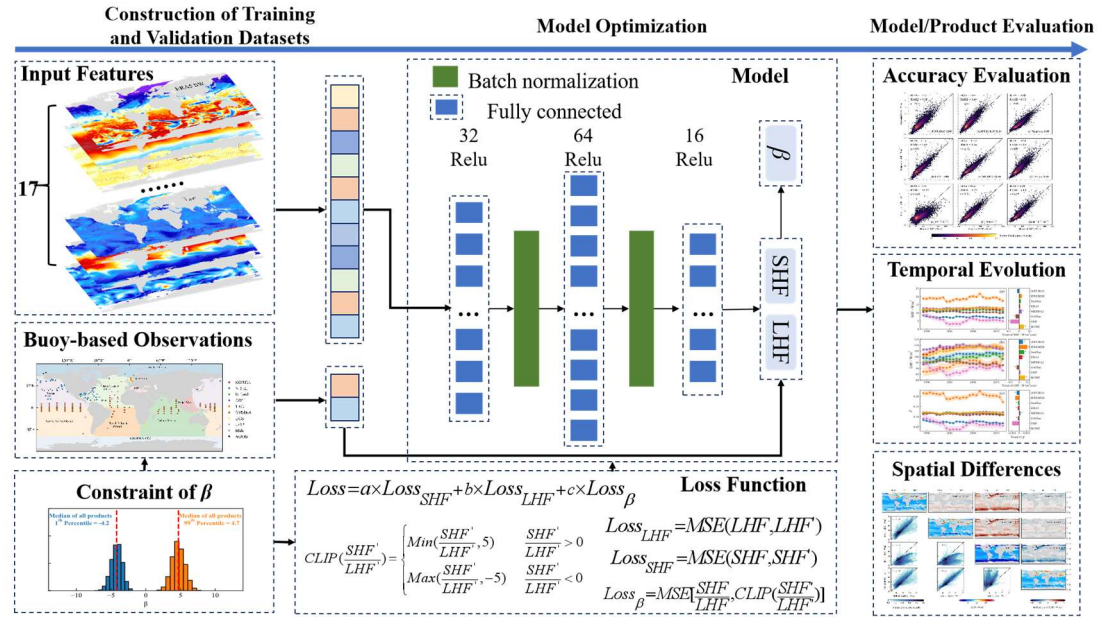
146 The primary objectives of this study are ~~three fold~~~~three folds~~: (1) to develop an
147 innovative ~~–Bowen ratio-constrained~~ statistical model for improving the air-sea SHF,
148 LHF and β estimates (referred to as the BrTHF model hereafter) using the machine
149 learning technique and global buoy-based air-sea turbulent heat fluxes observations; (2)
150 to demonstrate the superiority of the statistical model through an inter-comparison with
151 seven widely used global products and the estimates from the physics-free machine
152 learning-based model; (3) to produce a global daily 0.25° dataset based on the BrTHF
153 model over ice-free oceans covering the period from 1993 to 2017. The flux
154 observations from 197 global distributed buoys, along with multi-source satellite-based

155 and reanalysis-based forcing inputs, were collected to construct the models and further
 156 produce the global air-sea turbulent heat fluxes dataset. The accuracy and spatio-
 157 temporal patterns of the SHF, LHF and β estimates were inter-compared with seven
 158 widely used products, including the remote sensing-based JOFURO v3, IFREMER
 159 v4.1 and SeaFlux v3, as well as reanalysis-based ERA5 and MERRA2, hybrid-based
 160 OAFlux v3 and machine learning-based OHF v2 products.

161 2. Data and Methods

162 The following sub-sections provide an overview of the development of the BrTHF
 163 product, detailing the construction of air-sea turbulent heat fluxes observation datasets,
 164 learning forcing datasets and the BrTHF model, as well as the evaluation strategies used
 165 in this study, as indicated in Figure 1.





167

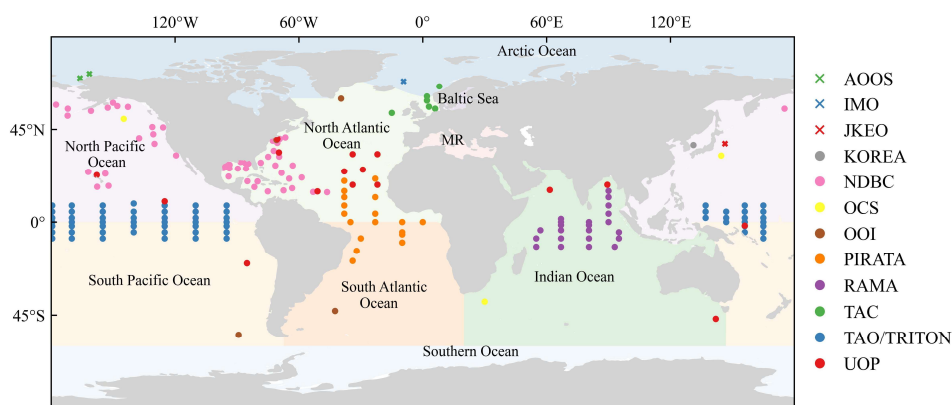
168 **Figure 1. flowchart of the generation of a global product of air-sea SHF, LHF and β by the**
 169 **BrTHF model**

170 **2.1 Air-sea turbulent heat fluxes observation datasets**

171 To obtain the buoy-derived air-sea turbulent heat fluxes observations, the hourly
 172 or sub-hourly oceanic and atmospheric measurements including sea surface
 173 temperature (T_s), sea surface air temperature (T_a), sea surface wind speed (WS) and
 174 relative humidity (RH) were firstly collected at 2687 buoys covering a variety of ocean
 175 basins from 13 organizations or networks, ~~namely 67 buoys from the Tropical~~
 176 ~~Atmosphere Ocean/Triangle Trans Ocean (TAO/TRITON) Buoy Network in the~~
 177 ~~Pacific, 20 buoys from the Prediction and Research Moored Array (PIRATA) in the~~
 178 ~~Atlantic, 23 buoys from the Research Moored Array for African-Asian-Australian~~
 179 ~~Monsoon Analysis and Prediction (RAMA) in the Indian Ocean, 73 buoys from~~
 180 ~~National Data Buoy Center (NDBC) around the coasts of the United States, 19 buoys~~
 181 ~~from Copernicus Marine In Situ Thematic Centre (TAC) nearby the coasts of Europe,~~
 182 ~~23 buoys from Upper Ocean Processes (UOP) Group around the low-latitude oceans~~
 183 ~~like the Bay of Bengal, 3 buoys from the Ocean Climate Stations Project (OCS) in the~~
 184 ~~mid-latitudes like the Kuroshio Extension, 24 buoys from Korea Meteorological~~
 185 ~~Administration (KOREA) nearby the Korean Peninsula, 6 buoys from Ocean~~

203 measurements (e.g. NDBC provided hourly observations before 2005 and 10-min
204 observations thereafter), we only retained the daily mean data when the fraction of the
205 valid hourly or sub-hourly observations exceeded 80% on a given day.

206 After the above mentioned data preprocessing, the daily buoy-derived air-sea
207 turbulent heat fluxes (SHF and LHF) observations were then calculated using the daily
208 oceanic and atmospheric measurements combined with the version 3.5 of Coupled
209 Ocean-Atmosphere Response Experiment (COARE3.5) model (Edson, 2013)
210 (available at <https://zenodo.org/record/5110991>). Although outliers of β exist in
211 observations, some are likely caused by measurement errors. Considering that such
212 outliers can severely impede model training and evaluation, it was necessary to
213 constrain β within a reasonable range to enable simultaneous high-accuracy estimation
214 of SHF, LHF, and β . Therefore, following the air-sea turbulent heat fluxes
215 computations, we further made a quality control on the derived SHF and LHF
216 observations to exclude the abnormal records, by filtering the observations based on
217 the range of daily β values determined from seven widely-used flux products.
218 Specifically, we calculated the cumulative distribution of daily β for each product and
219 their ensemble (across all products). The medians of the 1st and 99th percentiles,
220 approximately -5 and 5, respectively, were selected as the minimum and maximum of
221 valid daily β , as shown in Figure S1. In total, this study compiled 463,585 observations
222 of valid daily air-sea turbulent heat flux from 197 buoy stations (Figure 2 and Table S1)
223 in the Arctic Ocean, Pacific Ocean, Atlantic Ocean and Indian Ocean.



224
225 **Figure 2. Geographic locations of 197 buoy sites from 12 organizations or networks involved**

226 in this analysis including TAO/TRITON, PIRATA, RAMA, NDBC, TAC, UOP, OOI, AOO, S,
227 KOREA, OCS, JKEO and IMO. The boundaries of global land and open oceans were sourced
228 from the Natural Earth dataset (<https://www.naturalearthdata.com/downloads/>) and the
229 Global Oceans and Seas dataset (<https://www.marinerregions.org/sources.php>), respectively.
230 Abbreviations MR refers to the Mediterranean Region. It should be noted that the Caspian
231 Sea was not included within the boundaries of the open oceans and is shown in white.

232 Finally, the quality-controlled observations were collected to train and validate the
233 BrTHF model. Note that the COARE-based observations at the buoy stations have
234 already widely applied as a benchmark for global air-sea turbulent heat flux product
235 development and evaluation (Bentamy et al., 2017; Chen et al., 2020b; Tang et al., 2024;
236 Weller et al., 2022)

237 **2.2 Forcing Learning datasets and state-of-the-art products**

238 **2.2.1 Learning Forcing datasets for training the neural network**

239 Learning Forcing variables were carefully selected based on their potential
240 impacts on the variations of the air-sea turbulent heat fluxes (Grist et al., 2016;
241 Kudryavtsev et al., 2014; Myslenkov et al., 2021; Song, 2020, 2021; Yan et al., 2024)
242 to conduct the feature selection (see section 2.3.1). These variables include T_a , sea
243 surface air specific humidity (Q_a), Mean Sea Level Pressure (SLP), Downward Long
244 Wave Radiation Flux (LW), Downward Short Wave Radiation Flux (SW), T_s , sea surface
245 specific humidity (Q_s), Absolute Dynamic Topography (ADT), Sea Level Anomaly
246 (SLA), Sea Surface Salinity (SSS), Sea Surface Density (SSD), Ocean Mixed Layer
247 Current Velocity (CS), WS , Significant Wave Height (SWH), Wave period (T_p), as well
248 as gradient of temperature ($diff_T$) calculated using the T_s and T_a , and gradient of
249 humidity ($diff_Q$) calculated using the Q_s and Q_a .

250 ~~Datasets of these forcing variables were collected from the following sources~~
251 ~~(Table 1): the daily 0.25° ERA5 meteorology dataset (providing T_a , Q_a , SLP , LW and~~
252 ~~SW) (Hersbach et al., 2020) from the European Centre for Medium-Range Weather~~
253 ~~Forecasts (ECMWF) Climate Data Store (CDS), the daily 0.25° the Optimum~~

254 ~~Interpolation Sea Surface Temperature (OISST) dataset (T_s and Q_s) (Huang et al., 2021),~~
255 ~~the daily 0.25° Global Ocean Gridded L4 Sea Surface Heights And Derived Variables~~
256 ~~Reprocessed 1993 Ongoing (SSH) dataset (ADT and SLA), daily 0.125° Multi~~
257 ~~Observation Global Ocean Sea Surface Salinity and Sea Surface Density (MOGOSD)~~
258 ~~dataset (SSS and SSD) and 3-hour 0.2° Global Ocean Waves (GOW) Reanalysis dataset~~
259 ~~(SWH and T_p) from the Copernicus Marine Environmental Monitoring Service~~
260 ~~(CEMES), the daily 0.25° Ocean Surface Current Analysis Real-time (OSCAR) dataset~~
261 ~~(CS) (Bonjean and Lagerloef, 2002) from the Physical Oceanography Distributed~~
262 ~~Active Archive Center of the National Aeronautics and Space Administration (NASA)~~
263 ~~Jet Propulsion Laboratory (JPL), the 6-hour 0.25° Cross-Calibrated Multi-Platform~~
264 ~~(CCMP) wind vector analysis dataset (WS) from the Remote Sensing Systems~~
265 ~~(RSS).~~Datasets of these learning variables were collected from multiple publicly
266 available sources, as summarized in Table 2 and were used as the input features for
267 training the neural network.

268 The Multi Observation Global Ocean Sea Surface Salinity and Sea Surface
269 Density (MOGOSD) dataset~~MOGOSD~~ and Global Ocean Waves (GOW) Reanalysis
270 dataset~~GOW-datasets~~ were spatially resampled to a 0.25° resolution using mean
271 aggregation, while temporal mean aggregation to daily values was applied to the GOW
272 dataset (originally at 3-hour resolution) and Cross-Calibrated Multi-Platform (CCMP)
273 wind vector analysis dataset~~CCMP~~ (6-hour resolution)-~~datasets~~. Additionally, a daily
274 ERA5 sea-ice mask was applied to the datasets to mitigate the impact of sea ice.

275 **2.2.2 State-of-the-art products for inter-comparison**

276 Seven widely used air-sea turbulent heat fluxes products, involving remote
277 sensing-based JOFURO3, IFREMER and SeaFlux, as well as reanalysis-based ERA5
278 and MERRA2, hybrid-based OAFflux and machine learning-based OHF products were
279 selected for inter-comparison.

280 The remote sensing-based JOFURO3, IFREMER, and SeaFlux products were
281 developed by the Japanese Ocean Flux Data Sets under the Remote Sensing

282 Observations (J-OFURO) research project, the Institute Français de Recherche pour
283 l'Exploitation de la Mer (IFREMER), and the NASA Global Hydrology Resource
284 Center (GHRC) Distributed Active Archive Center (DAAC), respectively. The
285 reanalysis-based ERA5 and MERRA2 products were developed by the ECMWF and
286 NASA Global Modeling and Assimilation Office (GMAO), respectively. The hybrid-
287 based OAFflux and machine learning-based OHF products were developed or published
288 by the Woods Hole Oceanographic Institution (WHOI) and NOAA Ocean Surface
289 Bundle (OSB) Climate Data Record (CDR), respectively.

290 With the exception of the OHF product calculating SHF and LHF simultaneously
291 using a NN model without a constraint, all other products employed bulk aerodynamic
292 methods to estimate SHF and LHF. The JOFURO3, IFREMER, and OAFflux products
293 used the COARE3.0 model, while the SeaFlux used the COARE3.5 model. Differently,
294 the ERA5 adopted the bulk aerodynamic method used by the ECMWF, and the
295 MERRA2 used the method by the GEOS. These products provide SHF and LHF
296 estimates at a 0.25° spatial resolution, except for the MERRA2 ($0.5^\circ \times 0.625^\circ$) and
297 OAFflux (1°). Additionally, most products provide daily SHF and LHF estimates, while
298 only the OHF product provide estimates at a 3-hour interval. For further inter-
299 comparison, the daily mean aggregation was applied to the OHF products. More details
300 about the seven products can be found in the review of Tang et al. (2024).

Table 21 Summary of learning4foreing datasets used in this study

Dataset source	Resolution	Variables	Urls
ERA5	0.25°/daily	Sea surface air temperature (T_a), sea surface air specific humidity (Q_a), mean sea level pressure (SLP), downward long wave radiation flux (LN) and downward short wave radiation flux (SN)	https://cds.climate.copernicus.eu/datasets/derived-era5-single-levels-daily-statistics?tab=overview
OSCAR	0.25°/daily	Ocean mixed layer current velocity (CS)	https://podaac.jpl.nasa.gov/dataset/OSCAR_L4_OC_FINAL_V2.0
CCMP	0.25°/6-hour	Wind speed (WS)	https://data.remss.com/ccmp/v03.0/daily/
MOGOSD	0.125°/daily	Sea surface salinity (SSS) and sea surface density (SSD),	https://data.marine.copernicus.eu/product/MULTIOBS_GLO_PHY_S_SURFACE_MYNRT_015_013/description
SSH	0.25°/daily	Absolute dynamic topography (ADT) and sea level anomaly (SLA)	https://data.marine.copernicus.eu/product/SEALEVEL_GLO_PHY_CLIMATE_L4_MY_008_057/description
GOW	0.2°/3-hour	Significant wave height (SWH) and wave period (T_p)	https://data.marine.copernicus.eu/product/GLOBAL_MULTITYEAR_WAV_001_032/description
OISST	0.25°/daily	Sea surface temperature (T_s) and sea surface specific humidity (Q_s)	https://www.ncei.noaa.gov/data/sea-surface-temperature-optimum-interpolation/v2.1/access/avhrr/
OISST – ERA5	0.25°/daily	Gradient of temperature ($diff_T$) and gradient of humidity ($diff_Q$)	-

Table 32 Summary of the state-of-the-art air-sea turbulent heat fluxes products used for inter-comparison in this study

Dataset source	Resolution	Model	Variables	Urls
JOFURO3	0.25°/daily	COARE3.0		https://www.j-ofuro.com/en/
IFREMER	0.25°/daily	COARE3.0		ftp://ftp.ifremer.fr/ifremer/cersat/data/heat-flux/ifremer/v4.1/daily
SeaFlux	0.25°/daily	COARE3.5		https://www.earthdata.nasa.gov/data/catalog/ghrc-daac-seaflux-1
MERRA2	0.5° × 0.625°/daily	GEOS	Latent heat flux (LHF), sensible heat flux (SHF) and Bowen ratio (β = SHF/LHF)	https://developers.google.com/earth-engine/datasets/catalog/NASA_GSFC_MERRA_flux_2?hl=zh-cn#bands
ERA5	0.25°/daily	ECMWF	Bowen ratio (β = SHF/LHF)	https://cds.climate.copernicus.eu/datasets/derived-era5-single-levels-daily-statistics?tab=overview
OAFflux	1°/daily	COARE3.0		ftp://ftp.whoi.edu/pub/science/oaf Flux/data_v3
OHF	0.25°/3-hour	Neural Network model		https://www.ncei.noaa.gov/products/climate-data-records/ocean-heat-fluxes

306 2.3 Construction of the BrTHF model

307 2.3.1 Feature selection

308 The study employed a random forest (RF) model to evaluate the importance scores
309 of 17 oceanic and atmospheric ~~learning foreign~~ variables (with datasets collected in
310 Section 2.2) for target variables (SHF and LHF), aiming to filter out less influential
311 variables. As shown in Table S2, the variable importance assessment revealed that $diff_T$
312 and $diff_Q$ showed the highest importance score (71.56% and 49.93%) for SHF and LHF
313 modelling, respectively; additionally, WS exhibited the second highest importance for
314 both SHF (10.19%) and LHF (27.59%) modelling. Building upon the importance
315 evaluation and through careful screening of highly correlated variables, we ultimately
316 selected 11 key environmental features for subsequent air-sea turbulent heat fluxes
317 modelling including SLP , LW , SW , SSS , ADT , CS , WS , SWH , T_p , $diff_Q$, and $diff_T$.

318 2.3.1 Model construction and optimization

319 We selected the NN technique to build the BrTHF model due to its strong ability
320 to capture the complex nonlinear relationships between the multiple-inputs and
321 multiple-target variables with high accuracy (Zhou et al., 2024; Fu et al., 2023;
322 Cummins et al., 2023; Cummins et al., 2024). Additionally, the technique enables the
323 seamless integration of physical constraints, improving the reasonableness of the results
324 (Zhou et al., 2024; Zhao et al., 2019; Shang et al., 2023).

325 In order to estimate the SHF and LHF with high accuracy in a physics-consistency
326 framework, the β (= SHF/LHF) physical constraint was incorporated into the NN model
327 using the customed multiple-objects (SHF, LHF and β) loss function as follows:

$$328 \quad LOSS = a \times LOSS_{SHF} + b \times LOSS_{LHF} + c \times LOSS_{\beta} \quad (12)$$

329 $LOSS_{SHF}$, $LOSS_{LHF}$ and $LOSS_{\beta}$ represent the Mean Squared Error (MSE) of SHF, LHF and
330 β , respectively. They were weighted using the factors of a (SHF), b (LHF) and c (β) to
331 balance the different magnitudes of loss during optimization. To prevent potential
332 gradient explosion during model training, predicted β [SHF'/LHF' , calculated using the
333 predicted SHF (SHF') and LHF (LHF')] values were clipped within the observed range

334 of β (from -5 to 5) during training:

$$335 \quad CLIP\left(\frac{SHF'}{LHF'}\right) = \begin{cases} \text{Min}\left(\frac{SHF'}{LHF'}, 5\right) & \frac{SHF'}{LHF'} > 0 \\ \text{Max}\left(\frac{SHF'}{LHF'}, -5\right) & \frac{SHF'}{LHF'} < 0 \end{cases} \quad (23)$$

$$336 \quad Loss_{\beta} = MSE\left(\frac{SHF'}{LHF'}, CLIP\left(\frac{SHF'}{LHF'}\right)\right) \quad (34)$$

337 Finally, after optimization, the final weights (a, b and c) for SHF, LHF, and β were
338 set to 5, 1, and 250, respectively. The model was constructed consisting of one input
339 layer, three hidden layers, two BatchNormalization layers, and one output layer using
340 the Python TensorFlow library. The number of neurons in the three hidden layers were
341 32, 64, and 16, respectively and the activation function of Leaky Rectified linear unit
342 (ReLU) was used throughout the model.

343 To illustrate the superiority of the BrTHF model in terms of accuracy and physical
344 consistency, another physics-free NN models, trained without integrating the β
345 constraint, were also constructed to predict SHF and LHF separately for further
346 comparison, where β was calculated to be SHF/LHF.

347 **2.4 Evaluation strategy**

348 A spatial 10-fold cross-validation was employed to assess the performances of the
349 BrTHF model for estimating air-sea SHF, LHF and β . Compared to the traditional 10-
350 fold cross-validation, which randomly split all samples into ten folds and thus may
351 result in overlapping spatial samples between training and validating datasets, the
352 spatial 10-fold cross-validation were conducted in a relatively independent spatial
353 distribution and can provide a more generalized and convincing evaluation.

354 Specifically, first, all buoy sites were randomly split into ten folds. Then, each fold
355 was in succession selected as the validation dataset and the rest of ten folds was used
356 as the training dataset.

357 The metrics used to evaluate the performance of the models include: (1) the mean
358 bias error (BIAS); (2) the root mean squared error (RMSE); (3) the correlation
359 coefficient (r):

$$BIAS = \frac{1}{n} \sum_{i=1}^n (\hat{y}_i - y_i) \quad (45)$$

$$RMSE = \sqrt{\frac{1}{n} \sum_{i=1}^n (\hat{y}_i - y_i)^2} \quad (56)$$

$$r = \frac{\sum_{i=1}^n [(\hat{y}_i - \bar{\hat{y}})(y_i - \bar{y})]}{\sqrt{\sum_{i=1}^n (\hat{y}_i - \bar{\hat{y}})^2 \sum_{i=1}^n (y_i - \bar{y})^2}} \quad (67)$$

where n is the number of samples, \hat{y}_i and y_i are the estimated value and reference truth, $\bar{\hat{y}}$ and \bar{y} are the mean of \hat{y}_i and y_i , respectively. These metrics—BIAS, RMSE, and r —comprehensively evaluate model performance, representing systematic deviation, dispersion between observations and estimates, and the strength and direction of the linear relationship, respectively.

3. Results and discussion

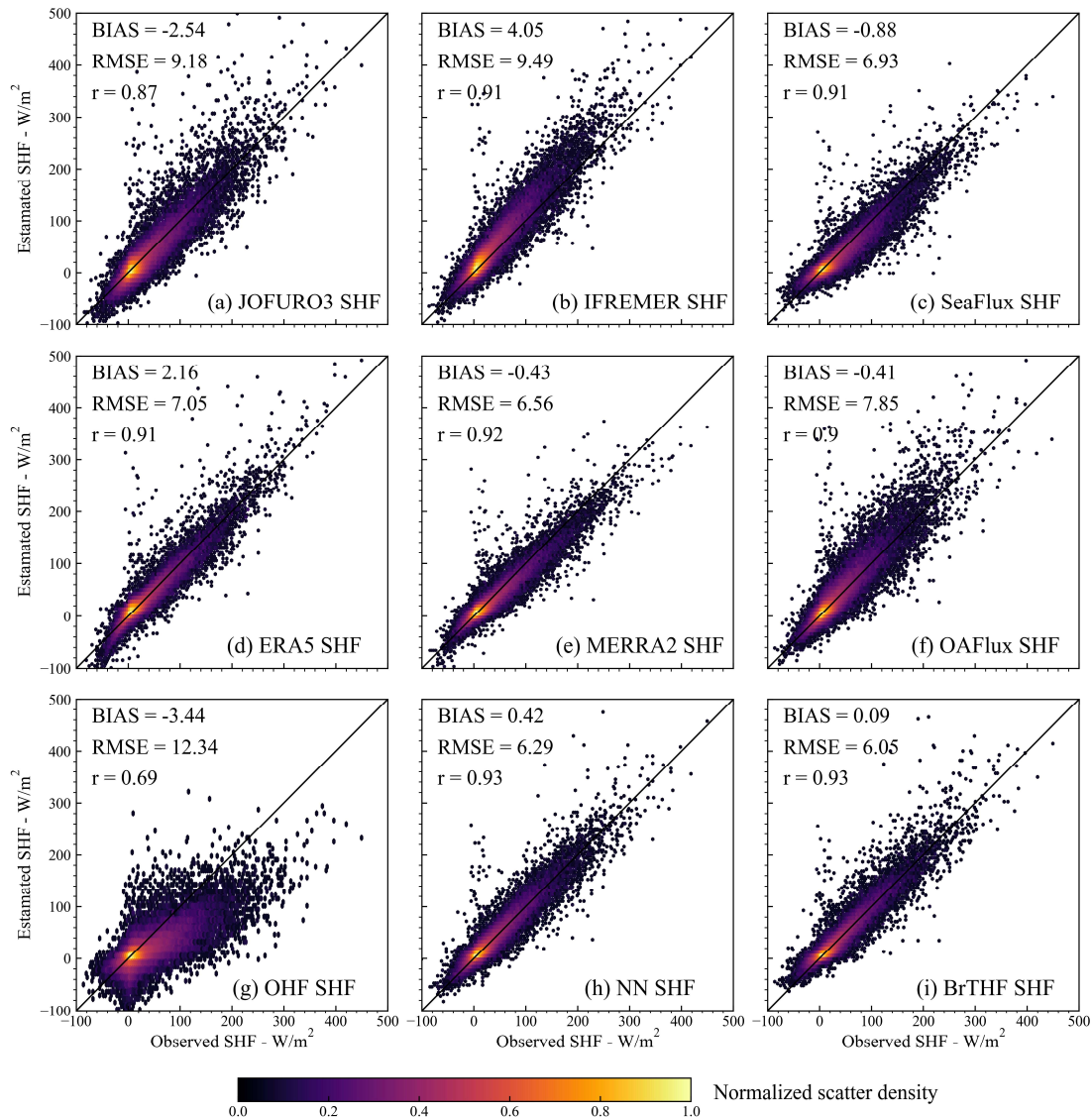
3.1 Spatial ten-fold cross-validation of the models

3.1.1 Overall accuracy

Figures 3, 4 and 5 present the normalized scatter density plots of the estimated daily SHF, LHF and β from the BrTHF and physics-free NN models, as well as the seven air-sea turbulent heat fluxes products against the observations obtained from 197 global distributed buoys by the spatial ten-fold cross-validation strategy.

Most models and products showed data distributions closely aligned with the observed SHF, with the majority of samples clustered around the 1:1 line. The BrTHF model slightly overestimated SHF with a BIAS of 0.09 W/m², whereas the physics-free NN models, ERA5 and IFREMER products showed more pronounced overestimations (from 0.42 W/m² to 4.05 W/m²). In contrast, the rest five products exhibited notable underestimations (from -3.44 W/m² to -0.41 W/m²). As illustrated in Figure 6, the variability of estimated SHF from the BrTHF and the physics-free NN models and ERA5 product closely matched the observed SHF, all with a Standard Deviation (STD) of approximately 16 W/m². Notably, the BrTHF model achieved the lowest RMSE (6.05 W/m²), outperforming both the physics-free NN models (6.29 W/m²) and the

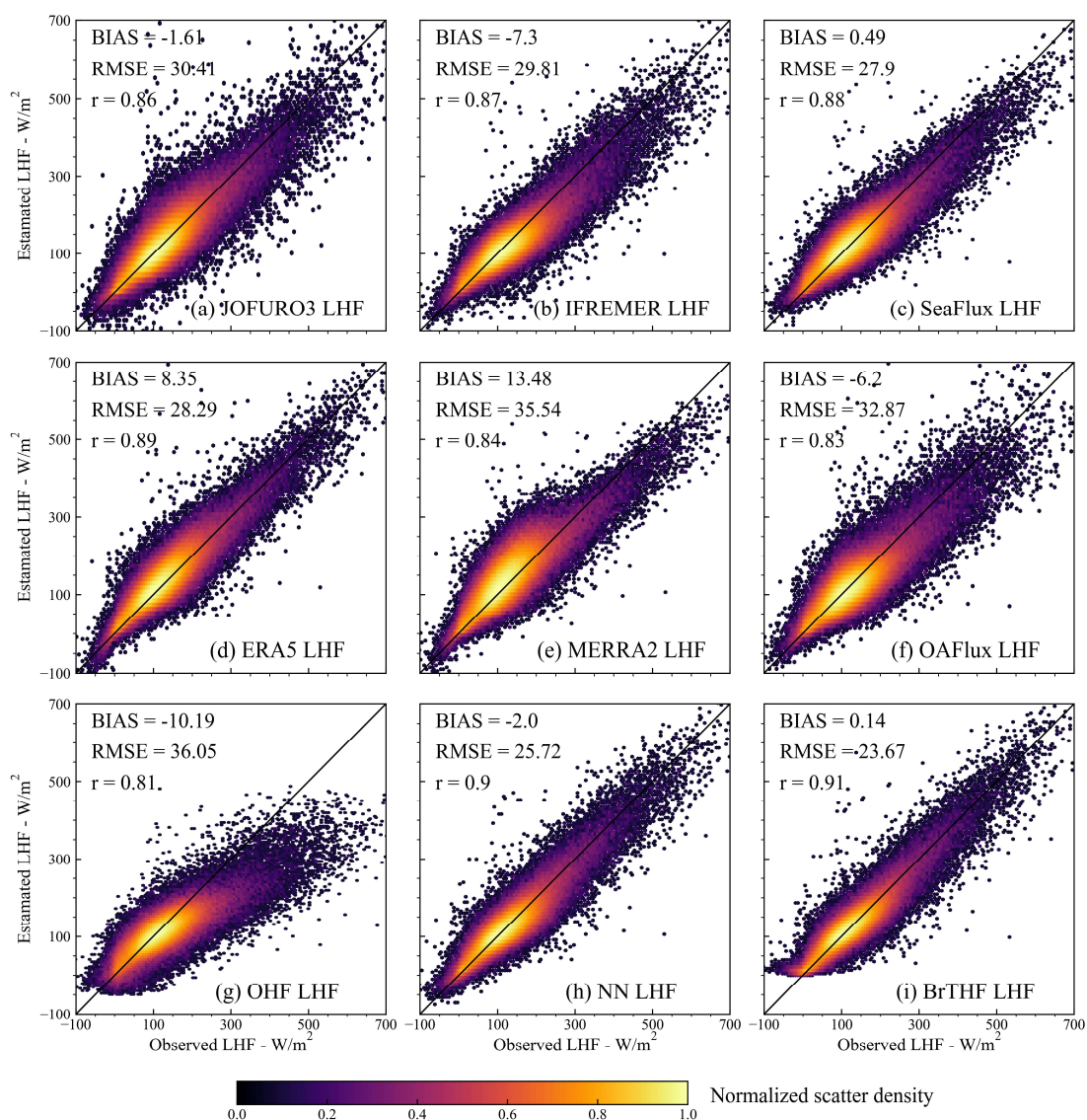
386 seven air-sea turbulent heat flux products (ranging up to 12.34 W/m^2 for OHF).
 387 Additionally, the BrTHF model combined with the physics-free NN models yielded the
 388 highest values of r (0.93), surpassing all seven other products. In summary, the BrTHF
 389 model showed overall the best performance in estimating SHF among all the models
 390 and products.



391
 392 **Figure 3. Normalized scatter density plots of estimated SHF from the BrTHF model, the**
 393 **physics-free NN models and seven air-sea turbulent heat fluxes products against the observed**
 394 **SHF obtained from 197 global distributed buoys.**

395 For LHF, similar to the results for SHF, the BrTHF model also demonstrated the
 396 best agreement with observations, achieving the lowest RMSE (23.67 W/m^2) and the

397 highest value of r (0.91). Compared to the physics-free NN models and seven products,
 398 the BrTHF model reduced RMSE by 2.05 W/m^2 (physics-free NN models) to 12.38
 399 W/m^2 (OHF) and improved r by 0.01 (physics-free NN model) to 0.1 (OHF).
 400 Additionally, the BrTHF model showed a slight overestimation of LHF (BIAS = 0.14
 401 W/m^2), lower than that of the SeaFlux, MERRA2, and ERA5 products. In contrast, the
 402 remaining products (JOFURO3, IFREMER, OAFflux, and OHF), along with the
 403 physics-free NN models, underestimated LHF, with the BIAS values ranging from -
 404 10.19 W/m^2 (OHF) to -1.61 W/m^2 (JOFURO3).



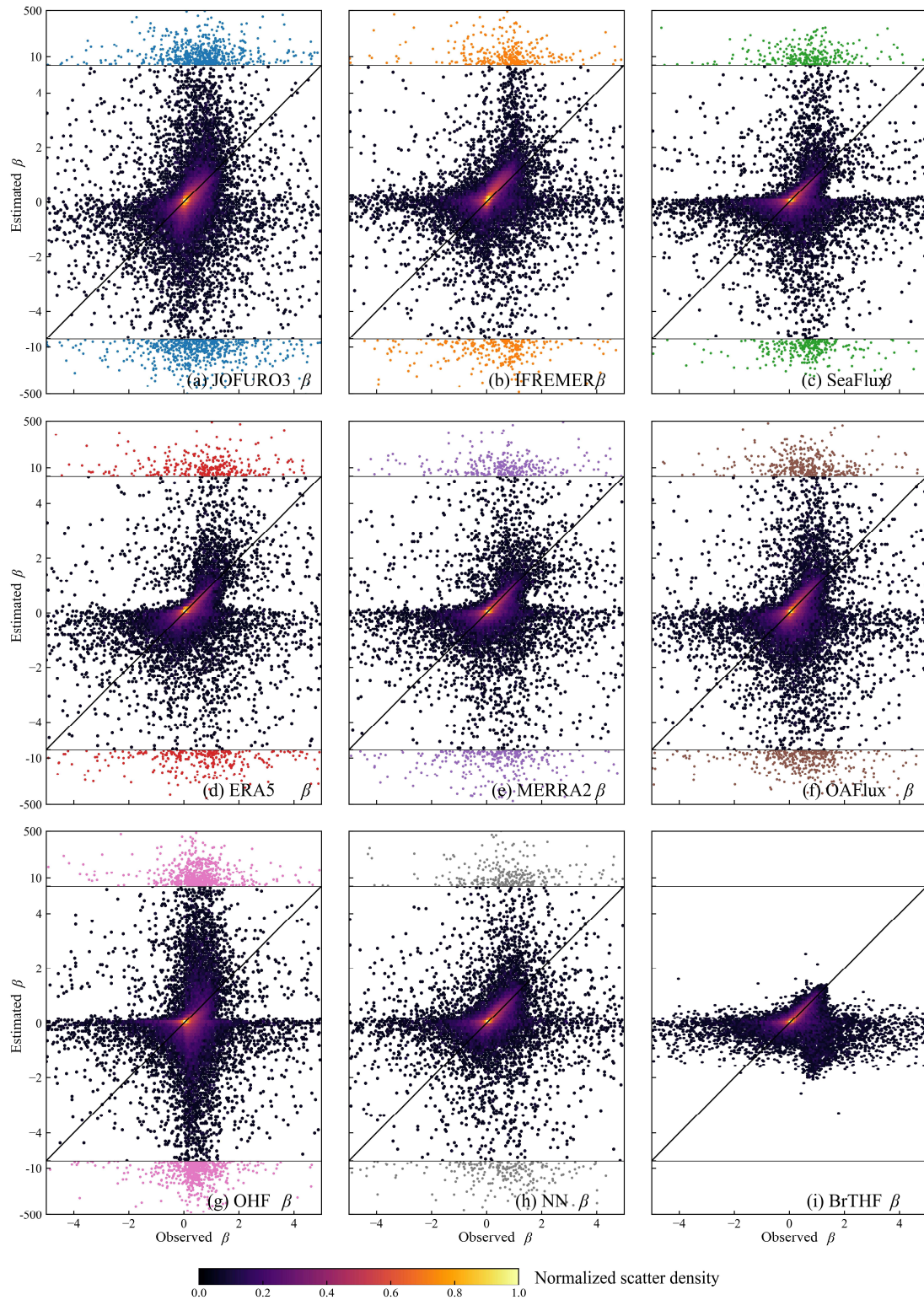
405

406 **Figure 4. Same as Figure 3 but for LHF.**

407

The BrTHF model exhibited a significantly different distribution of β compared to

408 the physics-free NN models and the seven products, as shown in Figure 5. The β
409 estimates from the BrTHF model consistently fell within the observed range of -5 to 5,
410 while the physics-free NN model and the seven products occasionally produced
411 estimates outside this range. Specifically, approximately 0.9% of β estimates from both
412 the physics-free NN model and the seven products were out of range. The extreme
413 positive and negative β estimates were found in the OHF ($\beta = 14997$) and physics-free
414 NN models ($\beta = -25703$) products, respectively. The abnormal β estimates significantly
415 impacted the accuracy of the physics-free NN models and the seven products as Figure
416 6 indicated. When excluding the abnormal β samples from the physics-free NN models
417 and seven products, the RMSEs ranged from 0.17 (physics-free NN models and
418 SeaFlux) and 0.26 (OHF), with values of r ranging from 0.13 (OHF) to 0.46
419 (IFREMER), as shown in Figure 6 and Table S3. However, when all estimates were
420 considered, the performances of these model and products deteriorated sharply, with
421 RMSEs rising from 0.87 (SeaFlux) to 39.21 (physics-free NN models), and values of r
422 dropping from 0.06 (SeaFlux) to 0 (JOFURO3, MERRA2 and OHF). In contrast, the
423 BrTHF model maintained robust outperformance, with the lowest RMSEs of 0.22 and
424 0.15, and higher r values of 0.25 and 0.43, both before and after removing the abnormal
425 β samples from the physics-free NN models and the seven products. Notably, the BIAS
426 values remained stable (ranging from -0.04 to 0.04) for all models and products,
427 regardless of whether the abnormal samples were excluded.



428

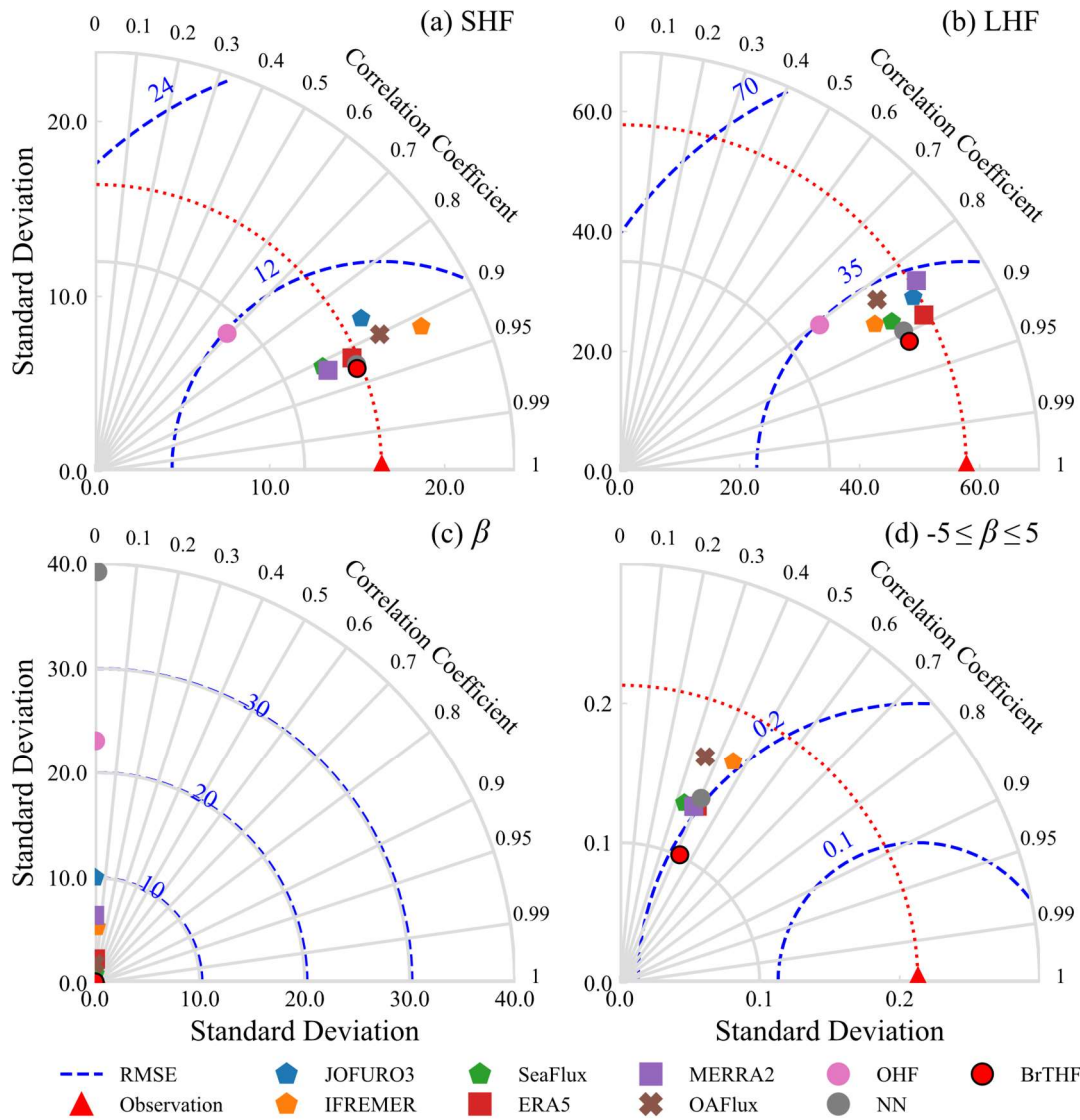
429

430

431

432

Figure 5. Same as [Figure 3](#) but for β . The samples out of the ranges of observed β ($-5 \leq \beta \leq 5$) were colored in blue, orange, green, red, purple, brown, pink and gray for JOFURO3, [IFREMER](#), SeaFlux, ERA5, MERRA2, OAFlux, OHF products and the physics-free NN models, respectively. [The statistical metrics could be found in Table S3 and Figure 6.](#)



433

434 **Figure 6. Taylor diagrams of the validation of estimated daily SHF (a), LHF (b), β (c) (-**
 435 **$5 \leq \beta \leq 5$, d) from the BrTHF model, the physics-free NN models and the seven products against**
 436 **the in-situ observations.**

437

438 3.1.2 Accuracies across oceans

439 To better understand the accuracy of SHF, LHF and β estimates from the BrTHF
 440 and physics-free NN models, as well as the seven products in different oceans, we
 441 conducted an additional evaluation by categorizing the observations according to the
 442 belonging ocean basins, as shown in Figure 7. The major ocean boundaries, obtained
 443 from Marine Regions (<https://www.marineregions.org/>), were used to define the ocean

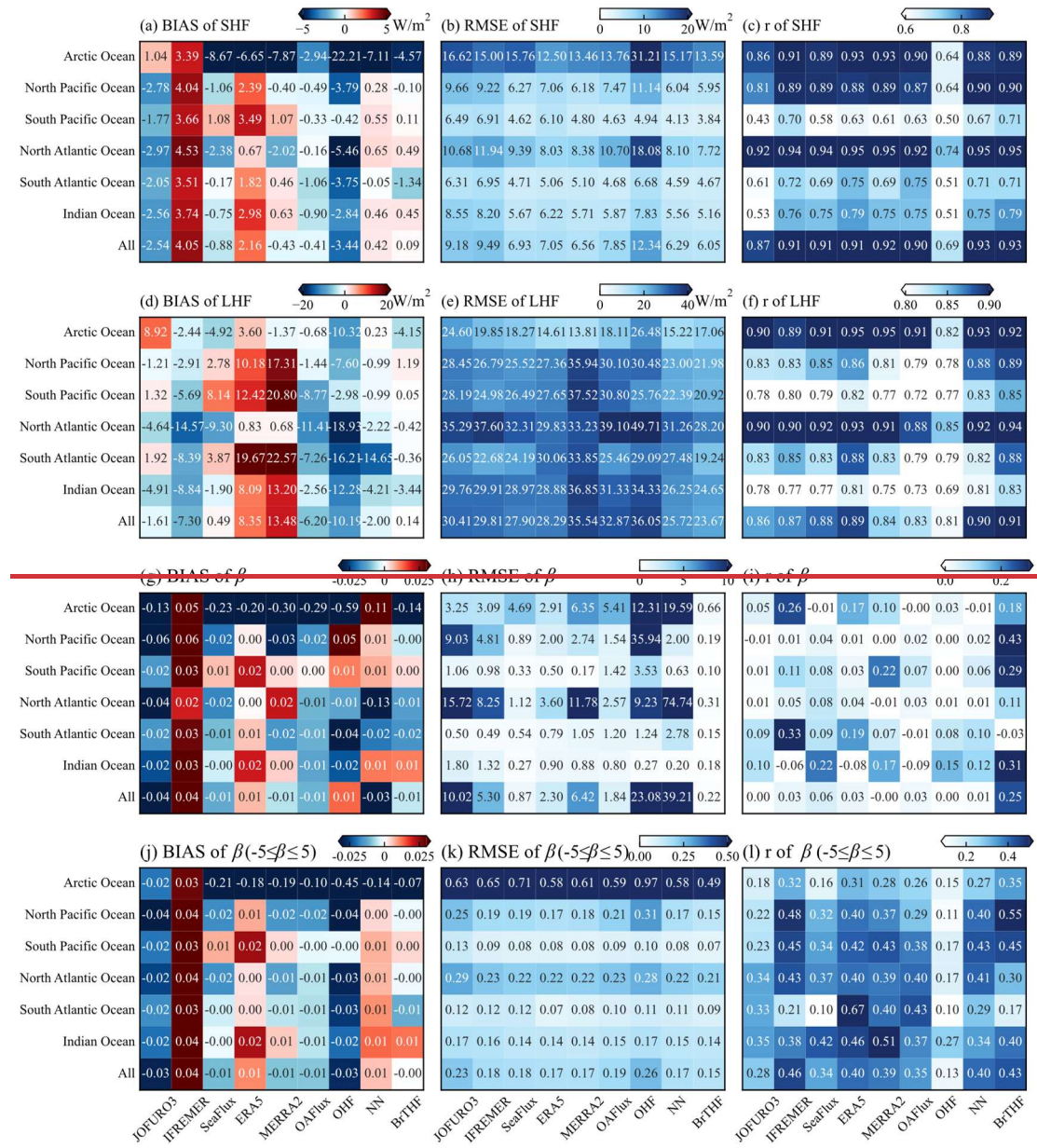
444 basins, which include the Arctic Ocean, South Pacific Ocean, North Pacific Ocean,
445 South Atlantic Ocean, North Atlantic Ocean, and Indian Ocean.

446 For SHF, the BrTHF model exhibited overestimations in the South Pacific Ocean,
447 North Atlantic Ocean, and Indian Ocean, while it underestimated SHF in the remaining
448 three ocean basins. The values of BIAS ranged from -4.57 W/m^2 in the Arctic Ocean to
449 0.49 W/m^2 in the North Atlantic Ocean. Furthermore, the BrTHF achieved the lowest
450 RMSEs in most ocean basins, ranging from 3.84 W/m^2 in the South Atlantic Ocean to
451 7.72 W/m^2 in the North Atlantic Ocean, except in the Arctic Ocean where the RMSE of
452 13.59 W/m^2 were higher than those of the ERA5 (12.5 W/m^2) and MERRA2 (13.46
453 W/m^2) products, as shown in Figure 7(b). Correlation analysis also demonstrated the
454 robust performance of the BrTHF model in estimating SHF, with values of r exceeding
455 0.89 in most ocean basins, except those ocean basins in the South Hemisphere (ranging
456 from 0.71 to 0.79) where the values of r for all models and products reduced.

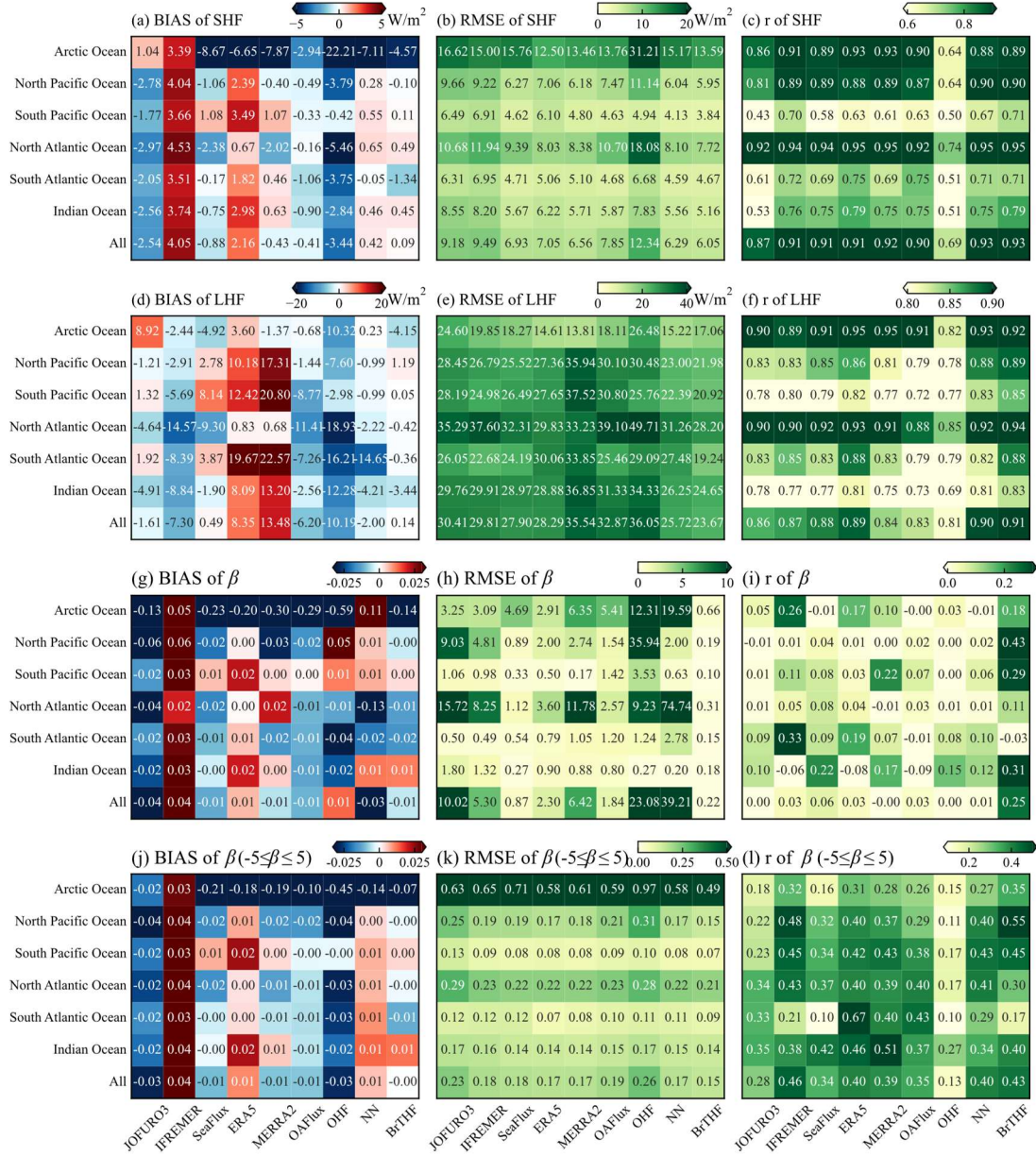
457 For LHF, the values of BIAS of the BrTHF model ranged from -4.15 W/m^2 in the
458 Arctic Ocean to 1.19 W/m^2 in the North Pacific Ocean. In comparison, the BrTHF
459 model showed more pronounced underestimations in the Arctic Ocean and Indian
460 Ocean. Additionally, the BrTHF model outperformed the physics-free NN models and
461 the seven products across most ocean basins, achieving the lowest RMSEs (ranging
462 from 17.06 W/m^2 in the Arctic Ocean to 28.20 W/m^2 in the North Atlantic Ocean) and
463 the highest values of r (ranging from 0.83 in the Indian Ocean to 0.94 in the North
464 Atlantic Ocean) except for the Arctic Ocean where the value of r was 0.01 less than the
465 physics-free NN models and the RMSE were 2.45 W/m^2 , 3.25 W/m^2 and 1.84 W/m^2
466 higher than the ERA5 and MERRA2 products and the physics-free NN models,
467 respectively.

468 The BrTHF model consistently performed better in estimating β across most ocean
469 basins, both before and after removing the abnormal β samples that deviated from the
470 observed range ($-5 \leq \beta \leq 5$). In contrast, the physics-free NN models and the seven
471 products did not perform as well. Specifically, the BrTHF model exhibited the lowest

472 RMSEs in almost all ocean basins except in the South Atlantic Ocean after removing β
 473 outliers. Moreover, in terms of correlation analysis, the BrTHF model achieved higher
 474 values of r in most ocean basins before and after the removal of abnormal β samples,
 475 among all models and products.



476



477

478 **Figure 7. Heatmaps of BIAS, RMSE and r metrics for the validation of estimated daily SHF**
 479 **(a - c), LHF (b - e), β (f - i) and $\beta (-5 \leq \beta \leq 5)$ (j - l) from the BrTHF model, the physics-free NN**
 480 **models and the seven products against the in-situ observations across different ocean basins.**

481 **It should be noted that the statistical metrics for each ocean basin were calculated using**
 482 **observations from the available buoys within the corresponding basin.**

483

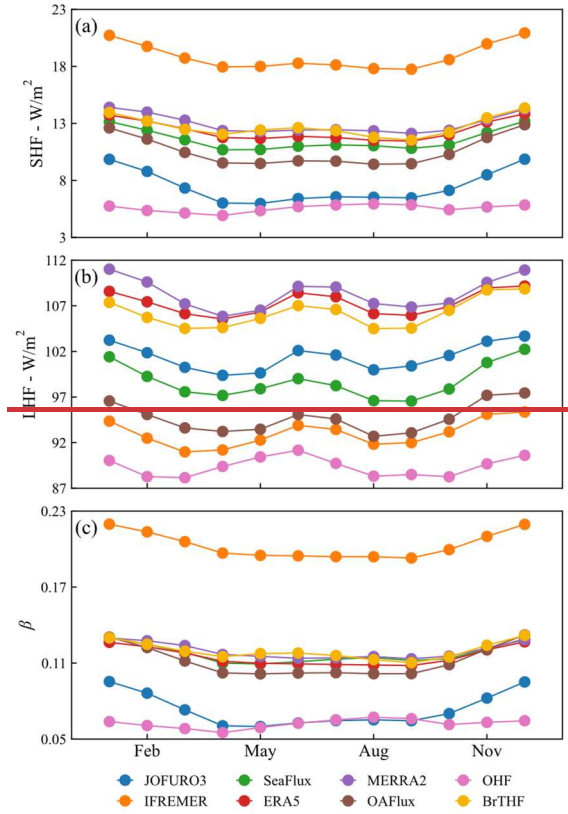
484 3.2 Temporal variations in SHF, LHF and β

485 After spatial ten-fold cross-validation, we produced the daily 0.25° global air-sea
 486 turbulent heat fluxes products from 1993 to 2017 using a combination of the BrTHF

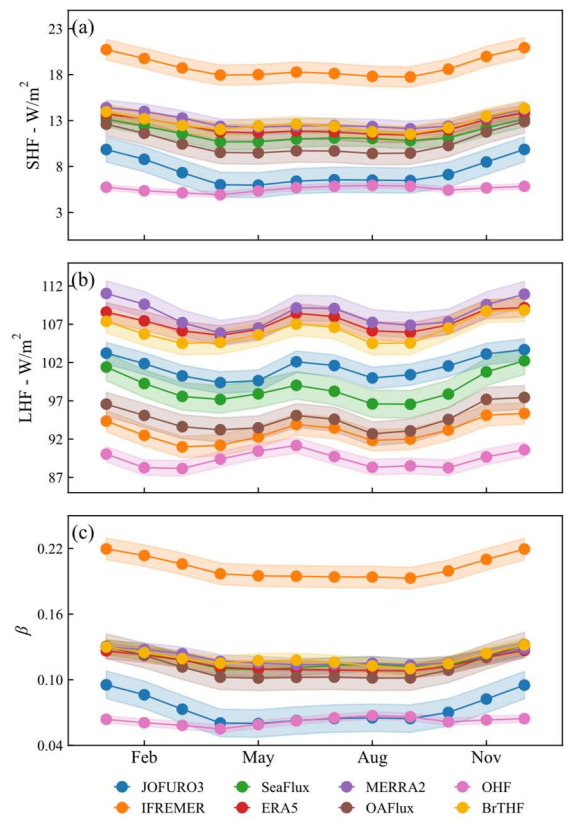
487 model and ~~foreign-learning~~ datasets, and further made a comparison of the temporal
488 variation (in this section), spatial distribution (in Section 3.3) and annual trend (in
489 Section 3.4) of SHF, LHF and β estimates from the BrTHF product and those with the
490 seven state-of-the-art global products. The selected period (from 1993 to 2017) was
491 determined by the overlapping availability of input ~~learning foreign~~ datasets.

492 Figure 8 illustrates the monthly area-weighted global means of SHF, LHF and β
493 from 1993 to 2017 for the BrTHF product and seven state-of-the-art products. The
494 BrTHF product exhibited similar bimodal patterns for SHF, LHF and β as the seven
495 products, with peaks in December-January and May-June-July-August. ~~However~~ In
496 addition, the peak in May-June-July-August was less pronounced for SHF and β
497 compared to that for LHF. The monthly area-weighted global means of SHF and β from
498 the BrTHF product were higher than those of most products, except for the MERRA2
499 product in January, February, March, April, July, August and September, and the
500 IFREMER product in all months. For LHF, the BrTHF showed lower values than the
501 ERA5 and MERRA2 products across all months. Notably, the patterns of SHF and β
502 from the OHF product, with the highest peak occurring in August and smoother intra-
503 annual cycles, differed from those of the corresponding BrTHF product and the other
504 six products developed using the bulk aerodynamic methods.

505



506



507

Figure 8. Intra-annual cycles of area-weighted global monthly mean of SHF (a), LHF (b) and

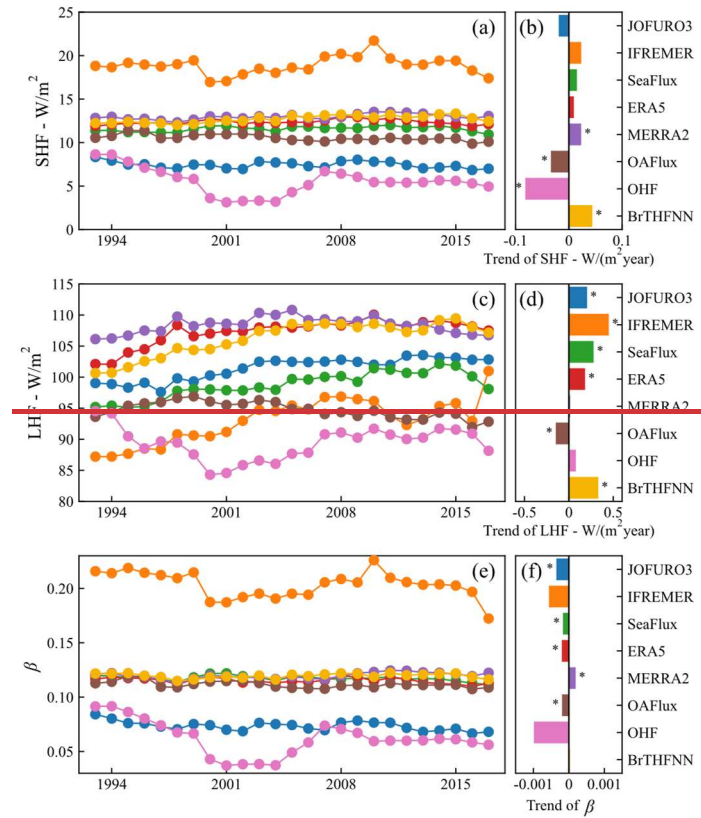
508

β (c) from the eight products from 1993 to 2017. The shaded areas indicate ± 1 standard

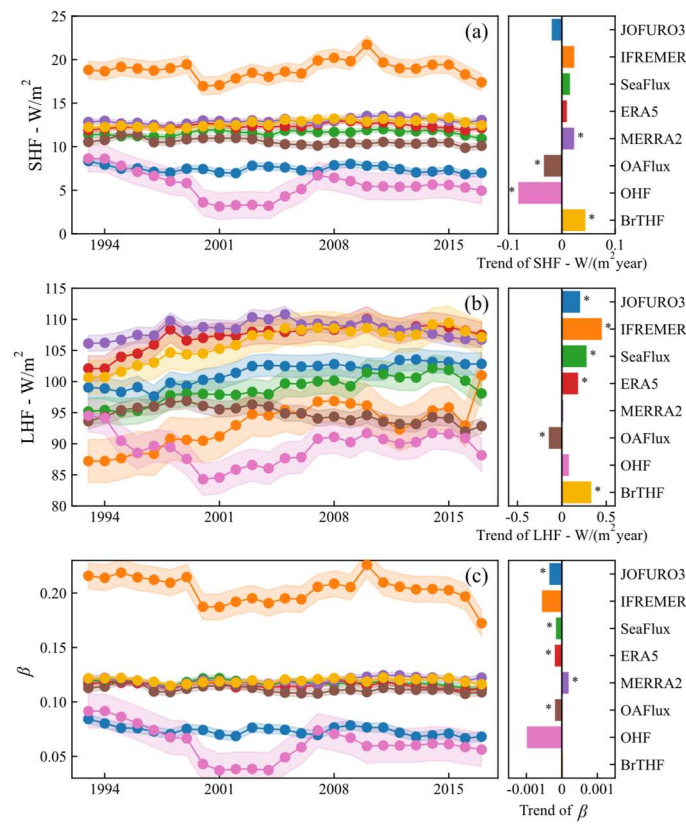
509 deviation around the mean.

510 Figure 9 presents the temporal evolution of the area-weighted annual global mean
511 of SHF, LHF and β from 1993 to 2017 for the eight products for the ice-free oceans.
512 The global mean annual SHF of the BrTHF product was 12.7 W/m^2 , which was close
513 to those of SeaFlux (11.6 W/m^2), OAFlux (10.6 W/m^2), MERRA2 (13 W/m^2) and
514 ERA5 (12.4 W/m^2), whereas significantly lower than that of IFREMER (18.8 W/m^2)
515 and higher than those of JOFURO3 (7.5 W/m^2) and OHF (5.6 W/m^2). Meanwhile, the
516 BrTHF product exhibited significant largest growth of SHF with the trend of 0.04
517 $\text{W}/(\text{m}^2\cdot\text{year})$ among all eight products, and showed similar temporal evolution as
518 SeaFlux, MERRA2, ERA5 and OAFlux during the period from 1993 to 2017. As for
519 LHF, the BrTHF exhibited a larger global mean annual value of 106.2 W/m^2 , which
520 was close to those of the ERA5 (107.3 W/m^2) and MERRA2 (108.3 W/m^2), and it was
521 significantly higher than ~~rest of the products~~the rest five products. Moreover, the growth
522 of the BrTHF LHF was significant with a trend of $0.33 \text{ W}/(\text{m}^2\cdot\text{year})$, which was lower
523 than the IFREMER but higher than the OAFlux, MERRA2, OHF, ERA5, JOFURO3
524 and SeaFlux, ranging from $-0.14 \text{ W}/(\text{m}^2\cdot\text{year})$ to $0.4 \text{ W}/(\text{m}^2\cdot\text{year})$. Note that only the
525 OAFlux product showed negative trend of LHF from 1993 to 2017. For β , the BrTHF
526 showed a similar temporal pattern to that of SHF, and most products concentrated
527 within the narrow range of 0.11 to 0.12 for the annual values. The magnitude of annual
528 β of the BrTHF was about 0.11, which was close to the OAFlux, SeaFlux, MERRA2
529 and ERA5, but significantly lower than the IFREMER and higher than the JOFURO3
530 and OHF. Moreover, in contrast to the significant increasing trends of LHF and SHF,
531 negative of trends of β were shown for most products. However, the BrTHF product
532 exhibited a weak positive trend, which may be attributed to the relatively smaller
533 differences between the SHF and LHF trends in BrTHF compared to those in other
534 products.

535



536



537 **Figure 9. Inter-annual evolution of area-weighted global mean SHF (a - b), LHF (c - d) and β**
 538 **(e - f) from 1993 to 2017. The trends were calculated based on the Sen's slope method. The ***

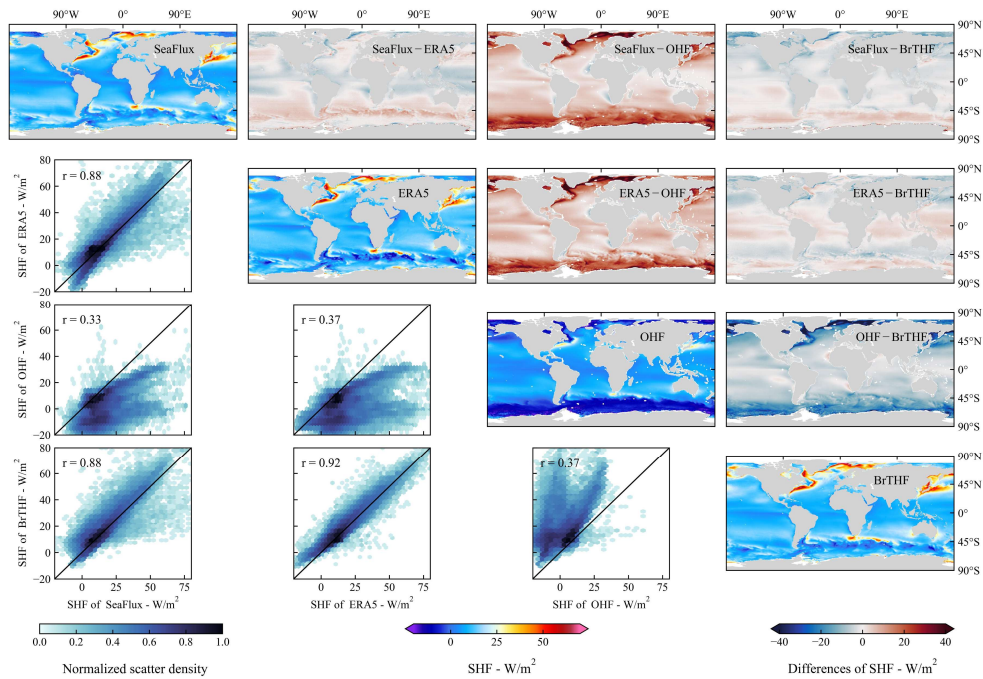
539 in the sub-figures (b, d and f) represent the trend passed the Mann-Kendall significant test (p
540 < 0.05). The shaded areas indicate ± 1 standard deviation around the mean.

541

542 3.3 Inter-comparison of the spatial pattern

543 We selected three representative products including the (reanalysis-based) ERA5,
544 (remote sensing-based) SeaFlux, and (the only publicly available machine learning-
545 based) OHF products to evaluate the BrTHF product's ability in simulating global air-
546 sea turbulent heat fluxes (SHF, LHF, and β) from 1993 to 2017. These products were
547 chosen because they demonstrated relatively high accuracy within their respective
548 categories (as shown in Section 3.1) and shared the same 0.25° spatial resolution with
549 the BrTHF product.

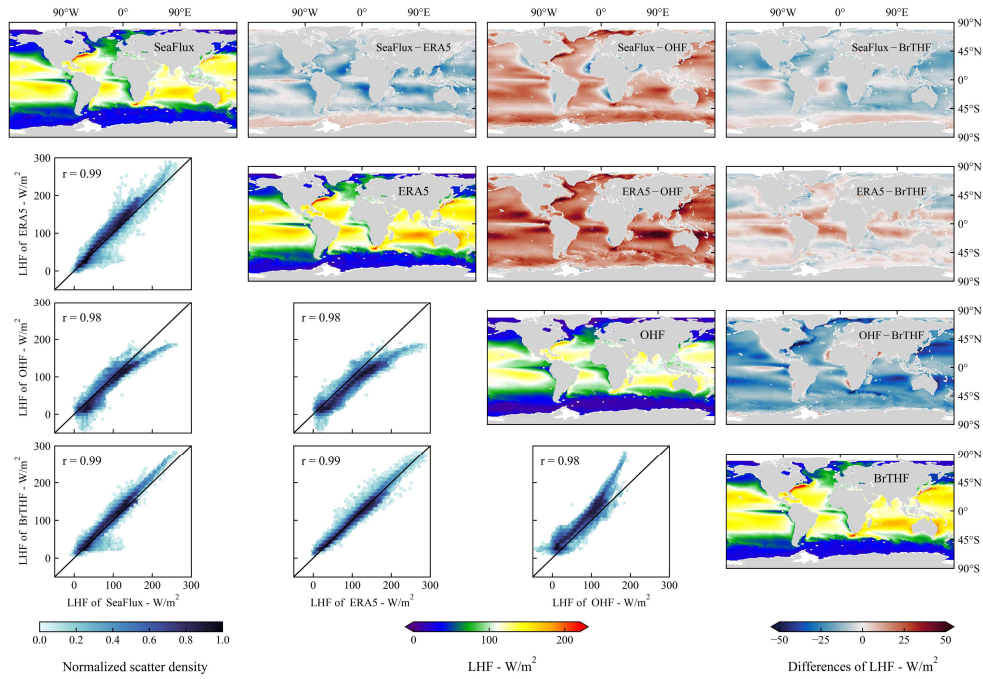
550 Figure 10 presents the spatial distribution of multi-year mean of SHF from the
551 SeaFlux, ERA5, BrTHF, and OHF products, along with their cross-comparisons.
552 Overall, the BrTHF product exhibited strong consistency with ERA5 and SeaFlux
553 products, with values of r exceeding 0.88, which was significantly higher than the
554 consistency between SeaFlux and OHF ($r = 0.33$) and between ERA5 and OHF ($r =$
555 0.37). Spatially, the BrTHF, SeaFlux and ERA5 products all showed higher SHF (over
556 50 W/m^2) in the Western Boundary Currents (WBCs, e.g. Kuroshio, Gulf Stream, Brazil
557 Current and Agulhas Current) regions, whereas OHF product yielded much lower SHF
558 ($\sim 25 \text{ W/m}^2$). Additionally, the former three products captured pronounced SHF
559 gradients in the Southern Ocean, features that were absent in OHF product. SHF
560 differences between BrTHF and SeaFlux/ERA5 remained within $\pm 10 \text{ W/m}^2$ in most
561 oceans. The BrTHF product exhibited slightly higher SHF values than SeaFlux in the
562 Northern Hemisphere, whereas in the Southern Hemisphere—particularly over the
563 Southern Ocean—the BrTHF showed relatively lower SHF. Compared to the ERA5
564 product, the BrTHF product yielded lower SHF in the equatorial zone, subtropical high-
565 pressure regions and the Southern Ocean, but higher SHF in other areas, particularly in
566 the North Pacific and the southern Indian Ocean.



567

568 **Figure 10. Inter-comparison of the spatial distributions of multi-year means of SHF among**
 569 **the SeaFlux, ERA5, OHF and BrTHF products from 1993 to 2017.**

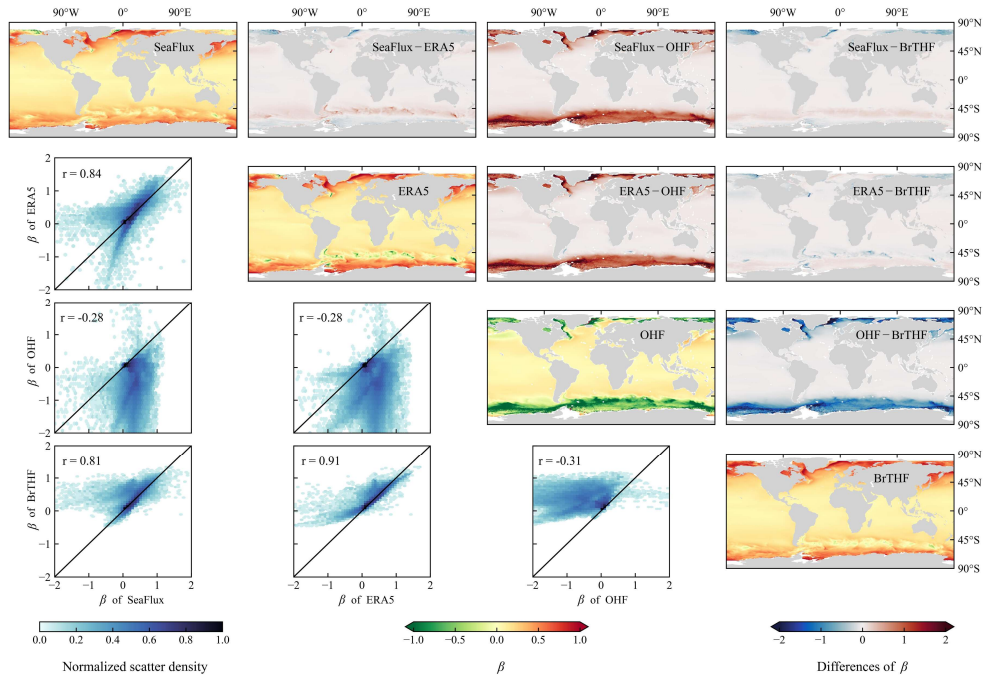
570 For LHF, the BrTHF and the selected three products exhibited more close spatial
 571 distribution patterns, with the values of r exceeding 0.98, compared to the results for
 572 the SHF, as shown in Figure 11. The higher LHF (over 150 W/m^2) primarily occurred
 573 around the regions of WBCs and the sub-tropic highs, while lower LHF (below 50
 574 W/m^2) appeared in the Eastern Equatorial Pacific and Atlantic Warm Tongue and the
 575 oceans with latitudes higher than 45° . The spatial distribution of LHF in the BrTHF
 576 product generally agreed better with that of the ERA5 product, though the BrTHF
 577 showed significantly lower LHF in sub-tropic highs. Additionally, the BrTHF exhibited
 578 relatively lower LHF than the ERA5 over the Southern Ocean and the central North
 579 Atlantic. Compared to the SeaFlux, the BrTHF yielded slightly higher LHF in most
 580 oceans except the Southern Ocean and equatorial zones.



581

582 **Figure 11. Same as Figure 10 but for LHF.**

583 For β , the BrTHF product demonstrated strong spatial correlation with the ERA5
 584 and SeaFlux in multi-year mean distributions, with values of r exceeding 0.81. In
 585 contrast, the OHF showed markedly a different spatial pattern of β , exhibiting negative
 586 correlations when compared to the rest of three products. Spatially, the BrTHF product's
 587 β distribution aligned more closely with the SeaFlux, both displaying higher β (up to 1)
 588 in high-latitude oceans particularly in the Northern Hemisphere and the similar
 589 wavelike textures of β over the Southern Ocean's Antarctic Circumpolar Current zone.
 590 The differences between the BrTHF and OHF products were more evident. Specifically,
 591 the BrTHF product showed overall overestimation of β in the oceans where latitudes
 592 were larger than 45° compared to the OHF product.



593

594 **Figure 12. Same as Figure 10 but for β .**

595

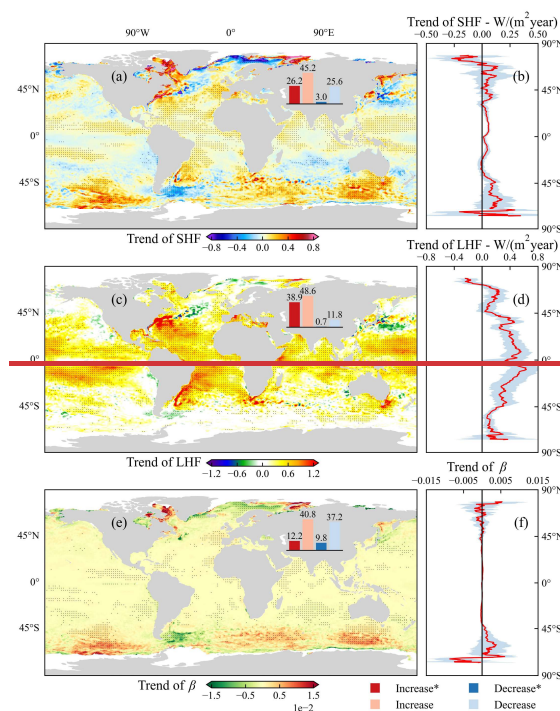
596 3.4 Spatial pattern of trends in SHF, LHF and β from the BrTHF product

597 Figure 13 illustrates the spatial distribution of inter-annual trends of SHF, LHF and
 598 β in the BrTHF product from 1993 to 2017. The SHF showed increasing trends across
 599 71.4% of the oceans, with statistically significant increases in 26.2% of regions. In
 600 contrast, decreasing trends were observed in 28.6% of the oceans, with only 3%
 601 showing significant reductions. Overall, the trends of zonal annual averages of SHF
 602 remained stable between the 60°N to 45°S, with significant increases occurring
 603 southward and decreases northward. Specifically, moderate increases (~ 0.2 W/(m²
 604 year)) dominated between 45°N and 45°S, while more pronounced increases (> 0.8
 605 W/(m² year)) were observed in high-latitude oceans, including the Kara Sea, Gulf
 606 Stream, Baffin Bay, Brazil Current, Sea of Okhotsk, and Sea of Japan. Notable
 607 decreases (< -0.8 W/(m² year)) were concentrated in the Barents Sea and the central
 608 North Atlantic.

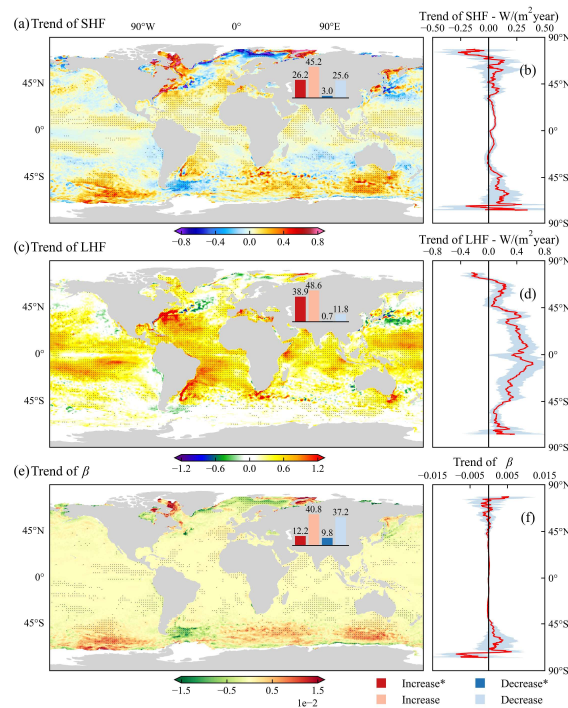
609 The LHF exhibited markedly different characteristics of the spatial distribution,
 610 with 87.5% of oceans showing increasing trends (38.9% were significant), versus 12.5%
 611 decreasing (0.7% were significant). In contrast to those of the SHF, the trends of zonal

612 annual averages for LHF weakened poleward from the oceans of Equator. The
 613 substantial increases ($>0.6 \text{ W/m}^2/\text{year}$) occurred in the oceans between 45°N to 45°S ,
 614 particularly in the Gulf Stream, Brazil Current, and Agulhas Current systems, while
 615 notable decreases (lower than $-0.3 \text{ W/m}^2/\text{year}$) were observed in the central North
 616 Atlantic and Kuroshio extension regions.

617 For β , approximately 53% of the oceans showed increasing trends, with 12.2% of
 618 these being statistically significant. Conversely, about 47% of the oceans showed
 619 decreasing trends, with 9.8% being significant. Most oceans between 45°N to 45°S
 620 exhibited near-zero trends, while significant trends were concentrated in the high-
 621 latitude oceans. Notable increases were found in Baffin Bay, Kara Sea, and the Southern
 622 Ocean, while decreases were observed in the Barents Sea and the Southern Ocean near
 623 South America.



624



625

626 **Figure 13. Spatial maps of inter-annual trends for SHF (a), LHF (c), and β (e) from the BrTHF**
 627 **product for the period 1993 to 2017. The trends were calculated using the Sen’s slope method.**
 628 **Dotted areas indicate oceans where the p-value of the Mann-Kendall significance test is less**
 629 **than 0.05. Panels (b), (d) and (f) represent the inter-annual trends of zonal annual averages**
 630 **for SHF, LHF and β , respectively.**

631 3.5 Discussion

632 Advancing our understanding of the air-sea interaction and achieving the global
 633 closure of the ocean surface energy budget require accurate global-scale simulations of
 634 air-sea turbulent heat fluxes (Yu, 2019). Existing global air-sea turbulent heat fluxes
 635 products, primarily generated using the semi-empirical bulk aerodynamic methods and
 636 data-driven machine learning approach, are often weak in accuracy and physical
 637 rationality, arising from uncertainties in environmental forcings and inappropriate
 638 parameterizations (Brodeau et al., 2017; Jiang et al., 2024a; Wang et al., 2024). To
 639 improve the simulation of the global air-sea turbulent heat fluxes, this study presents
 640 the BrTHF product, generated using a Bowen ratio-constrained NN technique with a
 641 customized multiple-objective loss function, as well as observations from 197 globally
 642 distributed buoys along with multi-source remote sensing and reanalysis foreign inputs.

643 The primary advantage of the BrTHF product is the absence of outliers in the
644 estimation of β . Unlike the approach of our previous study (Wang et al., 2024), which
645 simultaneously predicted SHF, LHF and β in the constructed RF model, this study
646 employed an NN model constrained by the Bowen ratio to jointly estimate SHF and
647 LHF. The new approach avoided the issue of selection of β derived from either the
648 calculated β [β_{cal} equals predicted SHF (SHF_{pre}) divided by predicted LHF (LHF_{pre})] or
649 the predicted β (β_{pre}), as reported by Wang et al. (2024). Furthermore, the customed loss
650 function in our new approach provides a flexible approach to adjust the weights of SHF,
651 LHF, and β , allowing the model to balance attention among these variables. As a result,
652 the accuracy of SHF, LHF, and β from our newly developed BrTHF model
653 outperformed that of the mainstream air-sea turbulent heat fluxes products and the
654 physics-free NN models on both global and regional scales. In contrast, the accuracy of
655 SHF and LHF in the model constructed by Wang et al. (2024) was somewhat marginally
656 lower than that of the physics-free RF model.

657 The machine learning-based OHF product demonstrated significantly poorer
658 performance in estimating SHF and LHF, with higher RMSEs and lower values of r , as
659 shown in Figure 6, compared to the remote sensing-, reanalysis-, and hybrid-based
660 products developed using the bulk aerodynamic methods. This finding contrasted with
661 the results of Tang et al. (2024), who reported the superior performance of the OHF
662 product. The discrepancy could primarily be attributed to the different spatial
663 representativeness of the observation datasets used by Tang et al. (2024), which were
664 primarily collected from the buoys between 30°N and 30°S. Moreover, as shown in
665 Figure 7, the accuracy of the OHF product degraded notably in high-latitude ocean
666 basins, particularly in the North Atlantic Ocean. This accuracy degradation may be due
667 to the limitation of the observation datasets used to train the model of the OHF product,
668 where different sources of datasets were integrated, i.e. the SeaFlux in-situ dataset
669 (before 2007) and the ICOADS in-situ dataset (after 2007). Specially, the ICOADS in-
670 situ datasets, commonly used for developing products at monthly or lower frequency

671 scales (Berry and Kent, 2011; Gulev et al., 2013), suffered from sparse distribution and
672 insufficient volume for developing the original 3-hour OHF product. Besides, the model
673 of the OHF product was trained by randomly splitting all observations into training,
674 validation, and test sets, which likely resulted in data dependencies across these sets,
675 weakening the model's transferability. These problems together contributed to the
676 poorer performance of the OHF product, including worse accuracy, overall negative
677 spatial trends in high-latitude oceans such as the Southern Ocean, as Tang et al. (2024)
678 reported, and an overall underestimation of the multi-year mean, especially in the
679 Western Boundary Currents (WBCs) where the air-sea exchange is intense. In addition,
680 the OHF product did not reproduce similar large-scale spatial patterns of air-sea
681 turbulent heat fluxes observed in BrTHF, ERA5, and SeaFlux, which are primarily
682 shaped by atmospheric circulation and sea surface properties (e.g., sea surface
683 temperature and salinity).

684 Based on Figure 2 and Table S8, we observe that the spatial coverage of
685 observations varies across different ocean regions: the Northern Hemisphere generally
686 has higher coverage than the Southern Hemisphere, with the Northern Pacific Ocean
687 exhibiting the highest coverage, while the Arctic Ocean shows the lowest. Comparing
688 spatial coverage with accuracy metrics reveals a more complex relationship between
689 model performance and data coverage. Specifically, the values of r tend to be lower in
690 regions with lower coverage — a pattern consistent across SHF, LHF, and β . However,
691 RMSE does not follow this trend. For SHF and β , RMSEs in the Northern Hemisphere
692 are generally higher than those in the Southern Hemisphere. Similarly, for LHF, RMSEs
693 are higher in the Northern Hemisphere except in the Indian Ocean, where the pattern
694 differs.

695 We applied a spatial 10-fold cross-validation, which provides a more generalized
696 assessment than traditional random cross-validation, to evaluate the BrTHF model.
697 However, it is important to acknowledge that the spatial distribution of the training
698 dataset is inherently imbalanced, with a heavy concentration of observations in the

699 Tropics and the Northern Hemisphere. In contrast, the Southern Hemisphere—
700 particularly the Southern Ocean—suffers from sparse or even missing observational
701 coverage. Given that the environmental conditions in these underrepresented or data-
702 sparse regions may differ significantly from those captured in the training dataset, the
703 selected input variables for the observations may lead to large uncertainty in the model's
704 performance in these areas. To further assess the model's ability to extrapolate to such
705 regions, we conducted an additional targeted cross-validation. Specifically, we
706 excluded stations from the Southern Ocean [i.e., Southern Ocean Flux Station (SOFS)
707 and Global Southern Ocean Station (GSOS)] from the training dataset and used them
708 solely for validation. Results presented in Tables S4 and S5 show that the BrTHF model
709 achieved the best performance in terms of LHF and β at the SOFS with lower RMSE
710 of 15.6 W/m² and 0.73 and higher values of r of 0.96 and 0.34, respectively, while its
711 SHF was slightly outperformed by ERA5 and the physics-free NN model. At the GSOS,
712 BrTHF yielded more accurate estimates for SHF and β with RMSEs of 6.38 W/m² and
713 0.74 and values of r of 0.95 and 0.16, respectively, compared to other products, while
714 its LHF was marginally less accurate than that of SeaFlux and the physics-free NN
715 model. Moreover, under both spatially-informed cross-validation and targeted cross-
716 validation, the model demonstrates comparable accuracy at the two sites, as shown in
717 Figures S4–S7. These findings suggest that BrTHF retains competitive accuracy of SHF,
718 LHF and β even in regions entirely excluded from training, reflecting promising
719 generalization. While these results are encouraging, it is important to note that the
720 validation remains limited to a small number of sites with available observations.
721 Therefore, the reported r values and RMSE reflect model performance in these specific
722 locations and do not necessarily guarantee similar accuracy in broader, unobserved
723 ocean regions.

724 The generalization capability of the model can also affect the accuracy of simulated
725 long-term trends. In Figure 13, we present the spatial distributions of long-term trends
726 for SHF, LHF, and β simulated by the BrTHF product. Considering the scarcity of

727 training data in high-latitude oceans, the simulated long-term trends in these regions
728 may be associated with larger uncertainties. However, due to the lack of long-term
729 observations in high-latitude oceans, we cannot validate the simulated trends using
730 observational records as has been done in previous studies for mid- and low-latitude
731 regions (Weller et al., 2022; Tang et al., 2024). To address this, we examined the spatial
732 distribution of long-term trends from the other seven widely used products. Specifically,
733 in these high-latitude regions, the trends simulated by the BrTHF are largely consistent
734 with those of most other products—for example, SHF exhibits a pronounced increase
735 in the Kara Sea, Gulf Stream, Baffin Bay, Brazil Current, Sea of Okhotsk, and Sea of
736 Japan, with differences mainly in magnitude.

737
738 Although the results demonstrated significant improvements in the accuracy and
739 physical consistency of SHF, LHF, and β estimates from the BrTHF model compared
740 to those from the physics-free NN models and the seven products, tThe BrTHF product
741 also has some limitations. First, due to the lack of an explicitly defined reasonable range
742 for daily β , the constraint of β used in this study was derived from the daily β global
743 distribution in the seven widely used global products. While incorporating the
744 constraint of β into the model effectively suppresses outliers, it also compresses the
745 physically plausible range of β . As a result, the distribution of β shown in Figure 5(i)
746 differs notably from other products and models, which may limit the product's
747 applicability for users interested in extreme β values. It is highlighted that although the
748 BrTHF model slightly underestimates the extreme values of β , it avoids the occurrence
749 of unrealistic outliers (e.g., 5 to 500 or -5 to -500) seen in other products, making it
750 overall better aligned with observations. Moving forward, we aim to enhance the
751 model's ability to preserve physically plausible extremes while maintaining robustness
752 against outliers in future updates.~~Although the results demonstrated significant~~
753 ~~improvements in the accuracy and physical consistency of SHF, LHF, and β estimates~~
754 ~~from the BrTHF model compared to those from the physics-free NN models and the~~

755 ~~seven products, there remains room for improvement once a more reasonable range for~~
756 ~~daily β is established.~~— Secondly, the estimated SHF and LHF values exhibited a
757 narrower distribution compared to the observations. This issue possibly stems from the
758 uncertainty of the BrTHF model that was constructed from the uneven distribution of
759 SHF and LHF in the observation datasets, which contain a low proportion of extreme
760 samples, especially negative LHF values. Moreover, due to the insufficient
761 observations, validation and modelling in high-latitude oceans, especially in the
762 Southern Ocean, was limited. To address these problems, more experiments are highly
763 recommended to collect observations covering more regions of oceans with better
764 spatial and temporal representativeness, which could further enhance the product.

765 The BrTHF model demonstrated the feasibility and potential of jointly estimating
766 multiple interrelated air-sea variables through a machine learning model that
767 incorporates appropriate physical constraints to account for their interrelations. In the
768 future, the predicted variables in the BrTHF model could be expanded to include
769 surface radiation, heat storage, and precipitation over the ocean, by integrating the
770 physical mechanisms of energy and water exchange. This would allow for the
771 collaborative optimization of estimates across all components of the air-sea energy and
772 water budgets, potentially contributing to achieving global closure of the air-sea energy
773 and water budgets.

774

775 **4. Data and code availability**

776 The daily 0.25° BrTHF product, consisting of SHF and LHF estimates from 1993
777 to 2017, can be freely accessed from the National Tibetan Plateau Data Center (TPDC)
778 [<https://doi.org/10.11888/Atmos.tpdc.302578>, Tang and Wang (2025)]. The code for
779 developing the product can be found on the GitHub platform
780 (<https://github.com/zhezhe1996/BrTHF>).

781

782 **5. Summary and Conclusion**

783 In this study, we generated a daily 0.25° air-sea turbulent heat fluxes product for
784 the period 1993 to 2017 using our developed BrTHF model and multi-source remote
785 sensing and reanalysis data. A comprehensive validation was performed against
786 observations from 197 buoys and inter-comparisons were made with seven
787 representative gridded products. The key findings are as follows:

788 The BrTHF model demonstrated the most significant improvement superior
789 accuracy in estimating the SHF, LHF and β , while its performance in estimating SHF
790 and LHF was generally comparable to or slightly better than that of the compared to
791 the physics-free NN models and the seven widely used air-sea turbulent heat products
792 (including the JOFURO3, IFREMER, SeaFlux, ERA5, MERRA2, OAFlux and OHF
793 products). Through the spatial ten-fold cross-validation against the observations from
794 the 197 buoys, the BrTHF model achieved RMSEs of 6.05 W/m^2 for SHF, 23.67 W/m^2
795 for LHF and 0.22 for β , and showed values of r of 0.93, 0.91, and 0.25 for SHF, LHF,
796 and β , respectively. Additionally, The BrTHF model performed better in evaluations
797 across six major ocean basins, with lower RMSEs and higher values of r , in comparison
798 to the physics-free NN models and the seven products. Notably, the BrTHF model
799 significantly improved the rationality of β estimates, successfully eliminating the
800 outliers observed in both the physics-free NN models and the seven products.
801 Furthermore, the global distributions for SHF, LHF, and β from the BrTHF product
802 closely matched those of the physically-based ERA5 and SeaFlux products. The global
803 mean annual estimates of SHF, LHF, and β from the BrTHF product from 1993 to 2017
804 were 12.7 W/m^2 , 106.2 W/m^2 and 0.11, respectively, all within the ranges of the seven
805 products. The BrTHF product exhibited similar intra-annual cycles for SHF, LHF and
806 β , with bimodal patterns featuring lower and higher peaks in May-June-July-August
807 and December-January, respectively, which was consistent with the results of the seven
808 state-of-the-art products. Additionally, the BrTHF product exhibited significant
809 increasing trends for global SHF and LHF, with rates of $0.04 \text{ W/(m}^2 \text{ year)}$ and 0.33
810 $\text{W/(m}^2 \text{ year)}$, respectively, which were consistent to most of the seven products. In

811 contrast, the BrTHF product displayed weak growth in β , with a trend approaching 0,
812 which were opposite to the results of the seven products except for the MERRA2
813 product. The increasing (significant increasing) trends dominated the oceans, with areas
814 of 71.4% (26.2%) for SHF, 87.5% (38.9%) for LHF, 53% (12.2%) for β in the BrTHF
815 product.

816 The BrTHF product shows significant advantages in the accuracy and rationality
817 of estimates for key parameters (SHF, LHF, and β) related to air-sea interaction and the
818 global energy and water budgets compared to the existing products. It holds great
819 potential for quantifying the global air-sea energy and water budgets, enhancing our
820 understanding of the air-sea interaction, and projecting climate change under global
821 warming.

822 **Author contribution**

823 YW and RT conceived the study and designed the experimental framework. YW
824 performed the experiment and prepared the initial manuscript draft. All authors
825 contributed to manuscript revision, and approved the final version of the manuscript.

826 **Competing interests**

827 The contact author has declared that none of the authors has any competing
828 interests.

829 **Acknowledgement**

830 We thank the flux datasets and [foreign learning](#) datasets provided by the J-OFURO
831 project, IFREMER, ECMWF, NASA, WHOI, NOAA, CEMES and RSS. Moreover,
832 we thank the observations provided by the TAO/TRITON, PIRATA, RAMA, NDBC,
833 TAC, UOP, OOI, AOOS, KOREA, OCS, JKEO and IMO networks or organizations.
834 This work is supported by the National Natural Science Foundation of China
835 [42271378,42071332], and the Strategic Priority Research Program of the Chinese
836 Academy of Sciences (Grant No. XDB0740202).

837

838 **References**

- 839 Andreas, E. L., Jordan, R. E., Mahrt, L., and Vickers, D.: Estimating the Bowen ratio
840 over the open and ice-covered ocean, *Journal of Geophysical Research: Oceans*,
841 118, 4334-4345, 10.1002/jgrc.20295, 2013.
- 842 Bentamy, A., Piollé, J. F., Grouazel, A., Danielson, R., Gulev, S., Paul, F., Azelmat, H.,
843 Mathieu, P. P., von Schuckmann, K., Sathyendranath, S., Evers-King, H., Esau, I.,
844 Johannessen, J. A., Clayson, C. A., Pinker, R. T., Grodsky, S. A., Bourassa, M.,
845 Smith, S. R., Haines, K., Valdivieso, M., Merchant, C. J., Chapron, B., Anderson,
846 A., Hollmann, R., and Josey, S. A.: Review and assessment of latent and sensible
847 heat flux accuracy over the global oceans, *Remote Sensing of Environment*, 201,
848 196-218, 10.1016/j.rse.2017.08.016, 2017.
- 849 Berry, D. I. and Kent, E. C.: Air-Sea fluxes from ICOADS: the construction of a new
850 gridded dataset with uncertainty estimates, *International Journal of Climatology*,
851 31, 987-1001, 10.1002/joc.2059, 2011.
- 852 Bonjean, F. and Lagerloef, G. S.: Diagnostic model and analysis of the surface currents
853 in the tropical Pacific Ocean, *Journal of Physical Oceanography*, 32, 2938-2954,
854 2002.
- 855 Bourras, D.: Comparison of five satellite-derived latent heat flux products to moored
856 buoy data, *Journal of Climate*, 19, 6291-6313, 2006.
- 857 Bourras, D., Eymard, L., and Liu, W. T.: A neural network to estimate the latent heat
858 flux over oceans from satellite observations, *International Journal of Remote*
859 *Sensing*, 23, 2405-2423, 10.1080/01431160110070825, 2002.
- 860 Bourras, D., Liu, W. T., Eymard, L., and Tang, W.: Evaluation of latent heat flux fields
861 from satellites and models during SEMAPHORE, *Journal of Applied Meteorology*,
862 42, 227-239, 2003.
- 863 Bourras, D., Reverdin, G., Caniaux, G., and Belamari, S.: A Nonlinear Statistical Model
864 of Turbulent Air-Sea Fluxes, *Monthly Weather Review*, 135, 1077-1089,
865 10.1175/mwr3335.1, 2007.
- 866 Bourras, D., Cambra, R., Marié, L., Bouin, M. N., Baggio, L., Branger, H., Beghoura,
867 H., Reverdin, G., Dewitte, B., Paulmier, A., Maes, C., Arduin, F., Pairaud, I.,
868 Fraunié, P., Luneau, C., and Hauser, D.: Air - Sea Turbulent Fluxes From a
869 Wave - Following Platform During Six Experiments at Sea, *Journal of*
870 *Geophysical Research: Oceans*, 124, 4290-4321, 10.1029/2018jc014803, 2019.
- 871 Bourras, D., Weill, A., Caniaux, G., Eymard, L., Bourlès, B., Letourneur, S., Legain,
872 D., Key, E., Baudin, F., Pignatelli, B., Traullé, O., Bouhours, G., Sinardet, B., Barrié,
873 J., Vinson, J. P., Boutet, F., Berthod, C., and Cléménçon, A.: Turbulent air - sea
874 fluxes in the Gulf of Guinea during the AMMA experiment, *Journal of*
875 *Geophysical Research: Oceans*, 114, 10.1029/2008jc004951, 2009.
- 876 Brodeau, L., Barnier, B., Gulev, S. K., and Woods, C.: Climatologically Significant
877 Effects of Some Approximations in the Bulk Parameterizations of Turbulent Air-
878 Sea Fluxes, *Journal of Physical Oceanography*, 47, 5-28, 10.1175/jpo-d-16-0169.1,

879 2017.

880 Brunke, M. A.: Uncertainties in sea surface turbulent flux algorithms and data sets,
881 *Journal of Geophysical Research*, 107, 10.1029/2001jc000992, 2002.

882 Cai, L., Wang, B., Wang, W., and Feng, X.: The Impact of Air–Sea Flux
883 Parameterization Methods on Simulating Storm Surges and Ocean Surface
884 Currents, *Journal of Marine Science and Engineering*, 13, 10.3390/jmse13030541,
885 2025.

886 Chen, X., Yao, Y., Zhao, S., Li, Y., Jia, K., Zhang, X., Shang, K., Xu, J., and Bei, X.:
887 Estimation of High-Resolution Global Monthly Ocean Latent Heat Flux from
888 MODIS SST Product and AMSR-E Data, *Advances in Meteorology*, 2020, 1-19,
889 10.1155/2020/8857618, 2020a.

890 Chen, X., Yao, Y., Li, Y., Zhang, Y., Jia, K., Zhang, X., Shang, K., Yang, J., Bei, X., and
891 Guo, X.: ANN-Based Estimation of Low-Latitude Monthly Ocean Latent Heat
892 Flux by Ensemble Satellite and Reanalysis Products, *Sensors (Basel)*, 20,
893 10.3390/s20174773, 2020b.

894 Clayson, C. and Brown, J.: NOAA Climate Data Record Ocean Surface Bundle (OSB)
895 Climate Data Record (CDR) of Ocean Heat Fluxes, Version 2, *Clim. Algorithm
896 Theor. Basis Doc. C-ATBD Asheville NC NOAA Natl. Cent. Environ. Inf. Doi*,
897 10, V59K4885, 2016.

898 Crespo, J., Posselt, D., and Asharaf, S.: CYGNSS Surface Heat Flux Product
899 Development, *Remote Sensing*, 11, 10.3390/rs11192294, 2019.

900 Cummins, D. P., Guemas, V., Cox, C. J., Gallagher, M. R., and Shupe, M. D.: Surface
901 Turbulent Fluxes From the MOSAiC Campaign Predicted by Machine Learning,
902 *Geophysical Research Letters*, 50, 10.1029/2023gl105698, 2023.

903 Cummins, D. P., Guemas, V., Blein, S., Brooks, I. M., Renfrew, I. A., Elvidge, A. D.,
904 and Prytherch, J.: Reducing Parametrization Errors for Polar Surface Turbulent
905 Fluxes Using Machine Learning, *Boundary-Layer Meteorology*, 190,
906 10.1007/s10546-023-00852-8, 2024.

907 Edson, J. B. a. J., Venkata and Weller, Robert A and Bigorre, Sebastien P and
908 Plueddemann, Albert J and Fairall, Christopher W and Miller, Scott D and Mahrt,
909 Larry and Vickers, Dean and Hersbach, Hans: On the Exchange of Momentum
910 over the Open Ocean, *Journal of Physical Oceanography*, 43, 1589-1610,
911 10.1175/jpo-d-12-0173.1, 2013.

912 Fasullo, J. T., Trenberth, K. E., and Balmaseda, M. A.: Earth’s Energy Imbalance,
913 *Journal of Climate*, 27, 3129-3144, 10.1175/jcli-d-13-00294.1, 2014.

914 Fu, S., Huang, W., Luo, J., Yang, Z., Fu, H., Luo, Y., and Wang, B.: Deep Learning -
915 Based Sea Surface Roughness Parameterization Scheme Improves Sea Surface
916 Wind Forecast, *Geophysical Research Letters*, 50, 10.1029/2023gl106580, 2023.

917 Gentemann, C. L., Clayson, C. A., Brown, S., Lee, T., Parfitt, R., Farrar, J. T., Bourassa,
918 M., Minnett, P. J., Seo, H., Gille, S. T., and Zlotnicki, V.: FluxSat: Measuring the
919 Ocean–Atmosphere Turbulent Exchange of Heat and Moisture from Space,
920 *Remote Sensing*, 12, 10.3390/rs12111796, 2020.

- 921 Grist, J. P., Josey, S. A., Zika, J. D., Evans, D. G., and Skliris, N.: Assessing recent air-
 922 sea freshwater flux changes using a surface temperature-salinity space framework,
 923 Journal of Geophysical Research: Oceans, 121, 8787-8806,
 924 10.1002/2016jc012091, 2016.
- 925 Gulev, S. K., Latif, M., Keenlyside, N., Park, W., and Koltermann, K. P.: North Atlantic
 926 Ocean control on surface heat flux on multidecadal timescales, Nature, 499, 464-
 927 467, 10.1038/nature12268, 2013.
- 928 Hersbach, H., Bell, B., Berrisford, P., Hirahara, S., Horányi, A., Muñoz - Sabater, J.,
 929 Nicolas, J., Peubey, C., Radu, R., Schepers, D., Simmons, A., Soci, C., Abdalla,
 930 S., Abellan, X., Balsamo, G., Bechtold, P., Biavati, G., Bidlot, J., Bonavita, M.,
 931 Chiara, G., Dahlgren, P., Dee, D., Diamantakis, M., Dragani, R., Flemming, J.,
 932 Forbes, R., Fuentes, M., Geer, A., Haimberger, L., Healy, S., Hogan, R. J., Hólm,
 933 E., Janisková, M., Keeley, S., Laloyaux, P., Lopez, P., Lupu, C., Radnoti, G.,
 934 Rosnay, P., Rozum, I., Vamborg, F., Villaume, S., and Thépaut, J. N.: The ERA5
 935 global reanalysis, Quarterly Journal of the Royal Meteorological Society, 146,
 936 1999-2049, 10.1002/qj.3803, 2020.
- 937 Huang, B., Liu, C., Banzon, V., Freeman, E., Graham, G., Hankins, B., Smith, T., and
 938 Zhang, H.-M.: Improvements of the Daily Optimum Interpolation Sea Surface
 939 Temperature (DOISST) Version 2.1, Journal of Climate, 34, 2923-2939,
 940 10.1175/jcli-d-20-0166.1, 2021.
- 941 Jiang, Y., Li, Y., Lu, Y., Wu, T., and Gao, Z.: Evaluating modifications to air-sea
 942 momentum flux parameterizations under light wind conditions in CAM6, Climate
 943 Dynamics, 62, 9687-9701, 10.1007/s00382-024-07415-8, 2024a.
- 944 Jiang, Y., Li, Y., Lu, Y., Wu, T., Zhang, J., and Gao, Z.: Evaluating nine different air-sea
 945 flux algorithms coupled with CAM6, Atmospheric Research, 10.1016/j.atmosres.2024.107486, 2024b.
- 947 Jo, Y.-H.: Calculation of the Bowen ratio in the tropical Pacific using sea surface
 948 temperature data, Journal of Geophysical Research, 107, 10.1029/2001jc001150,
 949 2002.
- 950 Karniadakis, G. E., Kevrekidis, I. G., Lu, L., Perdikaris, P., Wang, S., and Yang, L.:
 951 Physics-informed machine learning, Nature Reviews Physics, 3, 422-440, 2021.
- 952 Kashinath, K., Mustafa, M., Albert, A., Wu, J., Jiang, C., Esmailzadeh, S.,
 953 Azizzadenesheli, K., Wang, R., Chattopadhyay, A., and Singh, A.: Physics-
 954 informed machine learning: case studies for weather and climate modelling,
 955 Philosophical Transactions of the Royal Society A, 379, 20200093, 2021.
- 956 Kudryavtsev, V., Chapron, B., and Makin, V.: Impact of wind waves on the air - sea
 957 fluxes: A coupled model, Journal of Geophysical Research: Oceans, 119, 1217-
 958 1236, 10.1002/2013jc009412, 2014.
- 959 Liman, J., Schröder, M., Fennig, K., Andersson, A., and Hollmann, R.: Uncertainty
 960 characterization of HOAPS 3.3 latent heat-flux-related parameters, Atmospheric
 961 Measurement Techniques, 11, 1793-1815, 10.5194/amt-11-1793-2018, 2018.
- 962 Liu, Z. and Yang, H.: Estimation of Water Surface Energy Partitioning With a

- 963 Conceptual Atmospheric Boundary Layer Model, *Geophysical Research Letters*,
964 48, 10.1029/2021gl092643, 2021.
- 965 Loeb, N. G., Johnson, G. C., Thorsen, T. J., Lyman, J. M., Rose, F. G., and Kato, S.:
966 Satellite and Ocean Data Reveal Marked Increase in Earth's Heating Rate,
967 *Geophysical Research Letters*, 48, 10.1029/2021GL093047, 2021.
- 968 Monin, A. S. and Obukhov, A. M.: Basic laws of turbulent mixing in the surface layer
969 of the atmosphere, *Contrib. Geophys. Inst. Acad. Sci. USSR*, 151, e187, 1954.
- 970 Myslenkov, S., Shestakova, A., and Chechin, D.: The impact of sea waves on turbulent
971 heat fluxes in the Barents Sea according to numerical modeling, *Atmospheric
972 Chemistry and Physics*, 21, 5575-5595, 10.5194/acp-21-5575-2021, 2021.
- 973 Nelson, J. A., Walther, S., Gans, F., Kraft, B., Weber, U., Novick, K., Buchmann, N.,
974 Migliavacca, M., Wohlfahrt, G., Šigut, L., Ibrom, A., Papale, D., Göckede, M.,
975 Duveiller, G., Knohl, A., Hörtnagl, L., Scott, R. L., Zhang, W., Hamdi, Z. M.,
976 Reichstein, M., Aranda-Barranco, S., Ardö, J., Op de Beeck, M., Billesbach, D.,
977 Bowling, D., Bracho, R., Brümmer, C., Camps-Valls, G., Chen, S., Cleverly, J. R.,
978 Desai, A., Dong, G., El-Madany, T. S., Euskirchen, E. S., Feigenwinter, I.,
979 Galvagno, M., Gerosa, G. A., Gielen, B., Godeed, I., Goslee, S., Gough, C. M.,
980 Heinesch, B., Ichii, K., Jackowicz-Korczynski, M. A., Klosterhalfen, A., Knox, S.,
981 Kobayashi, H., Kohonen, K.-M., Korkiakoski, M., Mammarella, I., Gharun, M.,
982 Marzuoli, R., Matamala, R., Metzger, S., Montagnani, L., Nicolini, G., O'Halloran,
983 T., Ourcival, J.-M., Peichl, M., Pendall, E., Ruiz Reverter, B., Roland, M.,
984 Sabbatini, S., Sachs, T., Schmidt, M., Schwalm, C. R., Shekhar, A., Silberstein, R.,
985 Silveira, M. L., Spano, D., Tagesson, T., Tramontana, G., Trotta, C., Turco, F.,
986 Vesala, T., Vincke, C., Vitale, D., Vivoni, E. R., Wang, Y., Woodgate, W., Yepez,
987 E. A., Zhang, J., Zona, D., and Jung, M.: X-BASE: the first terrestrial carbon and
988 water flux products from an extended data-driven scaling framework,
989 *FLUXCOM-X, Biogeosciences*, 21, 5079-5115, 10.5194/bg-21-5079-2024, 2024.
- 990 O, S. and Orth, R.: Global soil moisture data derived through machine learning trained
991 with in-situ measurements, *Sci Data*, 8, 170, 10.1038/s41597-021-00964-1, 2021.
- 992 Peng, Z., Tang, R., Jiang, Y., Liu, M., and Li, Z.-L.: Global estimates of 500 m daily
993 aerodynamic roughness length from MODIS data, *ISPRS Journal of
994 Photogrammetry and Remote Sensing*, 183, 336-351,
995 10.1016/j.isprsjprs.2021.11.015, 2022.
- 996 Petersen, G. N.: Meteorological buoy measurements in the Iceland Sea, 2007–2009,
997 *Earth System Science Data*, 9, 779-789, 10.5194/essd-9-779-2017, 2017.
- 998 Robertson, F. R., Roberts, J. B., Bosilovich, M. G., Bentamy, A., Clayson, C. A., Fennig,
999 K., Schröder, M., Tomita, H., Compo, G. P., Gutenstein, M., Hersbach, H.,
1000 Kobayashi, C., Ricciardulli, L., Sardeshmukh, P., and Slivinski, L. C.:
1001 Uncertainties in Ocean Latent Heat Flux Variations over Recent Decades in
1002 Satellite-Based Estimates and Reduced Observation Reanalyses, *Journal of
1003 Climate*, 33, 8415-8437, 10.1175/jcli-d-19-0954.1, 2020.
- 1004 Shang, K., Yao, Y., Di, Z., Jia, K., Zhang, X., Fisher, J. B., Chen, J., Guo, X., Yang, J.,

1005 Yu, R., Xie, Z., Liu, L., Ning, J., and Zhang, L.: Coupling physical constraints with
1006 machine learning for satellite-derived evapotranspiration of the Tibetan Plateau,
1007 *Remote Sensing of Environment*, 289, 10.1016/j.rse.2023.113519, 2023.

1008 Shie, C.-L., Chiu, L. S., Adler, R., Nelkin, E., Lin, I. I., Xie, P., Wang, F.-C.,
1009 Chokngamwong, R., Olson, W., and Chu, D. A.: A note on reviving the Goddard
1010 Satellite-based Surface Turbulent Fluxes (GSSTF) dataset, *Advances in*
1011 *Atmospheric Sciences*, 26, 1071-1080, 10.1007/s00376-009-8138-z, 2009.

1012 Song, X.: The Importance of Relative Wind Speed in Estimating Air–Sea Turbulent
1013 Heat Fluxes in Bulk Formulas: Examples in the Bohai Sea, *Journal of Atmospheric*
1014 *and Oceanic Technology*, 37, 589-603, 10.1175/jtech-d-19-0091.1, 2020.

1015 Song, X.: The Importance of Including Sea Surface Current when Estimating Air–Sea
1016 Turbulent Heat Fluxes and Wind Stress in the Gulf Stream Region, *Journal of*
1017 *Atmospheric and Oceanic Technology*, 38, 119-138, 10.1175/jtech-d-20-0094.1,
1018 2021.

1019 Song, X., Xie, X., Yan, Y., and Xie, S.-P.: Observed sub-daily variations in air–sea
1020 turbulent heat fluxes under different marine atmospheric boundary layer stability
1021 conditions in the Gulf Stream, *Monthly Weather Review*, 10.1175/mwr-d-24-
1022 0003.1, 2024.

1023 TANG, R. and WANG, Y.: Global dataset of air-sea turbulent heat fluxes (sensible heat
1024 flux and latent heat flux) (1993–2017), National Tibetan Plateau Data Center
1025 [dataset], <https://dx.doi.org/10.11888/Atmos.tpdc.302578>, 2025.

1026 Tang, R., Wang, Y., Jiang, Y., Liu, M., Peng, Z., Hu, Y., Huang, L., and Li, Z.-L.: A
1027 review of global products of air-sea turbulent heat flux: accuracy, mean, variability,
1028 and trend, *Earth-Science Reviews*, 249, 10.1016/j.earscirev.2023.104662, 2024.

1029 Tomita, H., Hihara, T., Kako, S. i., Kubota, M., and Kutsuwada, K.: An introduction to
1030 J-OFURO3, a third-generation Japanese ocean flux data set using remote-sensing
1031 observations, *Journal of Oceanography*, 75, 171-194, 10.1007/s10872-018-0493-
1032 x, 2018.

1033 van der Westhuizen, S., Heuvelink, G. B., and Hofmeyr, D. P.: Multivariate random
1034 forest for digital soil mapping, *Geoderma*, 431, 116365, 2023.

1035 Wang, J., Tang, R., Jiang, Y., Liu, M., and Li, Z.-L.: A practical method for angular
1036 normalization of global MODIS land surface temperature over vegetated surfaces,
1037 *ISPRS Journal of Photogrammetry and Remote Sensing*, 199, 289-304,
1038 10.1016/j.isprsjprs.2023.04.015, 2023.

1039 Wang, Y., Tang, R., Huang, L., Liu, M., Jiang, Y., and Li, Z.-L.: A Bowen ratio-informed
1040 method for coordinating the estimates of air–sea turbulent heat fluxes,
1041 *Environmental Research Letters*, 19, 10.1088/1748-9326/ad9341, 2024.

1042 Weller, R. A., Lukas, R., Potemra, J., Plueddemann, A. J., Fairall, C., and Bigorre, S.:
1043 Ocean Reference Stations: Long-Term, Open-Ocean Observations of Surface
1044 Meteorology and Air–Sea Fluxes Are Essential Benchmarks, *Bulletin of the*
1045 *American Meteorological Society*, 103, E1968-E1990, 10.1175/bams-d-21-0084.1,
1046 2022.

1047 Wild, M., Folini, D., Hakuba, M. Z., Schär, C., Seneviratne, S. I., Kato, S., Rutan, D.,
1048 Ammann, C., Wood, E. F., and König-Langlo, G.: The energy balance over land
1049 and oceans: an assessment based on direct observations and CMIP5 climate
1050 models, *Climate Dynamics*, 44, 3393-3429, 10.1007/s00382-014-2430-z, 2014.

1051 Yan, Y., Song, X., Wang, G., and Li, X.: Tropical Cool-Skin and Warm-Layer Effects
1052 and Their Impact on Surface Heat Fluxes, *Journal of Physical Oceanography*, 54,
1053 45-62, 10.1175/jpo-d-23-0103.1, 2024.

1054 Yang, Y., Sun, H., Wang, J., Zhang, W., Zhao, G., Wang, W., Cheng, L., Chen, L., Qin,
1055 H., and Cai, Z.: Global ocean surface heat fluxes revisited: A new dataset from
1056 maximum entropy production framework with heat storage and Bowen ratio
1057 optimizations, *Earth System Science Data Discussions*, 2024, 1-44, 2024.

1058 Yu, L.: Global Air–Sea Fluxes of Heat, Fresh Water, and Momentum: Energy Budget
1059 Closure and Unanswered Questions, *Annual Review of Marine Science*, 11, 227-
1060 248, 10.1146/annurev-marine-010816-060704, 2019.

1061 Yu, L. and Weller, R. A.: Objectively Analyzed Air–Sea Heat Fluxes for the Global Ice-
1062 Free Oceans (1981–2005), *Bulletin of the American Meteorological Society*, 88,
1063 527-540, 10.1175/bams-88-4-527, 2007.

1064 Zhang, R., Guo, Weihao, Wang, Xin, and Wang, Chunzai: Ambiguous Variations in
1065 Tropical Latent Heat Flux since the Years around 1998, *Journal of Climate*, 36,
1066 3403–3415, 2023.

1067 Zhao, W. L., Gentine, P., Reichstein, M., Zhang, Y., Zhou, S., Wen, Y., Lin, C., Li, X.,
1068 and Qiu, G. Y.: Physics - Constrained Machine Learning of Evapotranspiration,
1069 *Geophysical Research Letters*, 46, 14496-14507, 10.1029/2019gl085291, 2019.

1070 Zhou, S., Shi, R., Yu, H., Zhang, X., Dai, J., Huang, X., and Xu, F.: A Physical -
1071 Informed Neural Network for Improving Air - Sea Turbulent Heat Flux
1072 Parameterization, *Journal of Geophysical Research: Atmospheres*, 129,
1073 10.1029/2023jd040603, 2024.

1074 Zhou, X., Ray, P., Barrett, B. S., and Hsu, P.-C.: Understanding the bias in surface latent
1075 and sensible heat fluxes in contemporary AGCMs over tropical oceans, *Climate
1076 Dynamics*, 55, 2957-2978, 10.1007/s00382-020-05431-y, 2020.

1077